# Development of an Integrated Geological-Engineering Framework for Assessing the Heat Extraction Potential from the Geopressured Wilcox Reservoir on the Gulf Coast of Texas

Kartik Mawa[1], Mojdeh Delshad[1], Marcos Vitor Barbosa Machado[2], Shuvajit Bhattacharya[3], and Peter Eichhubl[3]

[1] Hildebrand Department of Petroleum and Geosystems Engineering, The University of Texas at Austin
[2] Petrobras
[3] HotRock Geothermal, Bureau of Economic Geology, The University of Texas at Austin

**Keywords:** Geothermal energy; geopressured geothermal; Wilcox sandstone; Non-isothermal reservoir simulation.

## Abstract

This study aims to establish a comprehensive framework for evaluating the geothermal potential of High-Pressure and High-Temperature (HPHT) aquifers or geopressured geothermal reservoirs in the Wilcox Formation on the onshore Gulf Coast of Texas, USA. The framework integrates geological and engineering approaches to determine the feasibility and viability of harnessing geothermal energy from these aquifers. By considering geological features and reservoir properties, such as heat capacity and thermal conductivity of fluid and rock, fluid flow dynamics, and heat losses in the wellbore and through the under and overburden, this integrated framework will provide valuable insights for the sustainable production of geothermal resources from the onshore Wilcox aquifers.

## Introduction

There has been a significant increase in exploration, pilot-scale demonstration, and further research in geothermal energy in the US and world. The Gulf Coast of Texas and Louisiana is known for its geopressured geothermal reservoirs.

Over the years, several studies have been published on the regional geothermal potential of the Gulf Coast at a regional scale (Bebout et al., 1979; Esposito and Augustine, 2012; Richards and Blackwell, 2012; Batir and Richards, 2020a and 2020b; Bhattacharya et al., 2022). Esposito and Augustine (2012) at NREL assessed the potential of onshore geopressured geothermal energy from the Gulf Coast. The Bureau of Economic Geology at the University of Texas Austin led a department of Energy-funded project to drill two pilot test wells (Pleasant

Bayou 1 and 2) in Brazoria County in 1978. The brine along with co-produced methane was used to generate electricity (Riney, 1991). Recently, geothermal startups, such as Sage Geosystems, have started exploring the hot, dry rocks (HDR) on the Gulf Coast (Texas Railroad Commission Press Release, 2025).

The objective of this study is to understand the effect of geologic complexities (such as faults), well geometry, well placement, fluid injection rate, and working fluid type ($CO_2$ and water) on hot brine production from deep reservoirs. We also perform sensitivity analysis of various well geometry parameters. Till date, there have been very few studies on the Gulf Coast regarding detailed reservoir engineering and simulation aspects of these geopressured reservoirs for heat production. The study is organized into a few sections: geologic modeling, dynamic non-isothermal characterization, sensitivity studies.

Numerous studies have been conducted to compare the effect of $CO_2$ (commonly known as $CO_2$ plume geothermal) instead of $H_2O$ as the working fluid for thermal power generation. (Ganjdanesh et al. 2012; Liu et al. 2015). s$CO_2$ has often been coined as a better working fluid than water for thermodynamic efficiency of the former fluid. For a given driving pressure, $CO_2$ has approximately 4 times the mass flow and 1.5 times the net heat recovery rate of water. (Wu et. al. 2020).

However, there have been differences between these studies. While the net heat recovery rate and the mass productivity of $CO_2$-EGS were higher than that of $H_2O$-EGS, Pritchett (2009) found that for the same conditions, the heat extraction efficiency was the greatest when using water as the working fluid. The $CO_2$ thermosiphon design for thermal extraction and power generation has been considered as an alternative to $H_2O$-EGS. The system was evaluated by Atrens et al. (2009). They concluded that there was less thermal recovery from the $CO_2$ thermosiphon as compared to the $H_2O$ system.

A combination of CCS with geothermal generation has been proposed for Wilcox, however, our simulation models focus majorly on generation of heat by injecting $CO_2$ instead of $H_2O$. That being stated, $CO_2$-based closed-loop geothermal systems will have a different output.

## Geological Modeling

The study area is located on the Gulf Coast. The geology of the Gulf Coast basin is complex due to rapid sedimentation, syn-depositional growth faults, and salt domes. Several regional-scale extensional faults are present on the Gulf Coast as shown in Figure 1 (Frio, Vicksburg, Wilcox fault zones). Most of these regional faults are oriented NE-SW, whereas there are some cross-faults along NW-SE and salt detachment related faults are present. As a result of continued

sedimentation, porous sandstone reservoirs were displaced downward and came in contact with impermeable shale layers across the fault, which resulted in the development of potential reservoirs in the Gulf Coast formations. Wilcox is divided into three intervals: lower, middle and upper depositional systems. The primary reservoirs in the Lower Wilcox are dense, piled high-energy river sandstones. A higher proportion of fine-grained, floodplain-derived shales, which operate as a regional pressure compartmentalizer and thermal insulator, exists in the Middle Wilcox, and a stratigraphic linkage to the Carrizo Formation above appears when the Upper Wilcox transitions to a sand-dominated phase (Hargis, 1985).

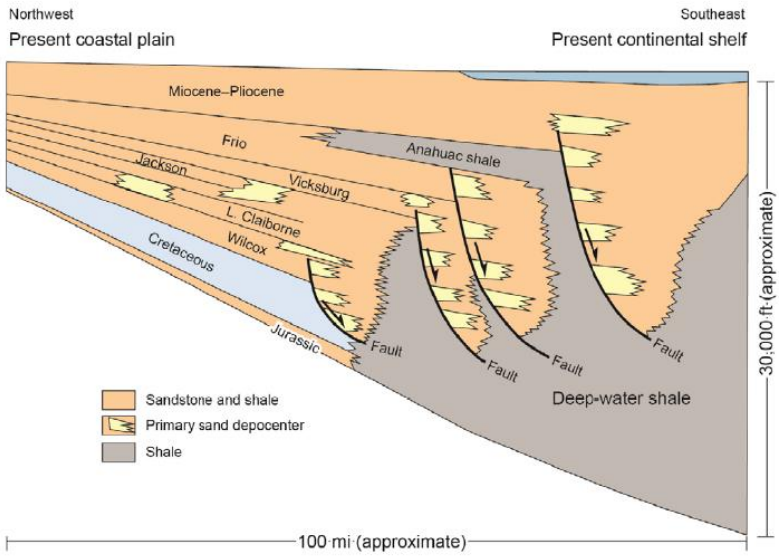


**Figure 1:** Schematic cross-section through the central area of the Texas Gulf Coast. Source: Adapted from Land and Fisher, 1987.

The Wilcox Group's structural complexity is primarily ascribed to growth faulting and depositional tectonic activity, which have impacted fluid storage and heat retention. The isolated pressure compartments that result from growth fault connections along the Gulf Coast have enhanced the potential of Wilcox sand bodies for geothermal heat storage. Owing to the higher-than-normal pressure gradients seen in these faulted reservoirs, geopressured fluids may accumulate. Many geothermal fairways have been restricted by faults that align with hydrocarbon resources that were previously thoroughly defined below the surface. Long-term thermal reservoirs with negligible convective heat loss occur when thick shale intervals within high-permeability sandstones additionally hinder vertical fluid migration (Bebout et al., 1979).

## Petrophysical Modeling

The reservoir quality of Wilcox vertically and laterally is controlled by facies, structures, and burial depth. The onshore Wilcox in certain locations has 5%-40% porosity, 0.01-10,000 mD permeability, and a high net-to-gross thickness below supercritical depth, and different depositional environment, facies (i.e., rock type) and burial depth exhibit a varied range of petrophysical properties. Lower Wilcox sandstones underwent burial diagenesis and created micro-porosity with low permeability (Loucks and Dutton, 2019). A major portion of the upper Wilcox contains freshwater-to-brackish water (Bhattacharya et al., 2023). Figure 2 shows the Wilcox core samples and Figure 3 provides the mineralogy of upper and lower Wilcox. The porosity and permeability distributions are representative of the Wilcox per Figure 4.

**Figure 2:** An example of varying Wilcox facies from a lower Wilcox core

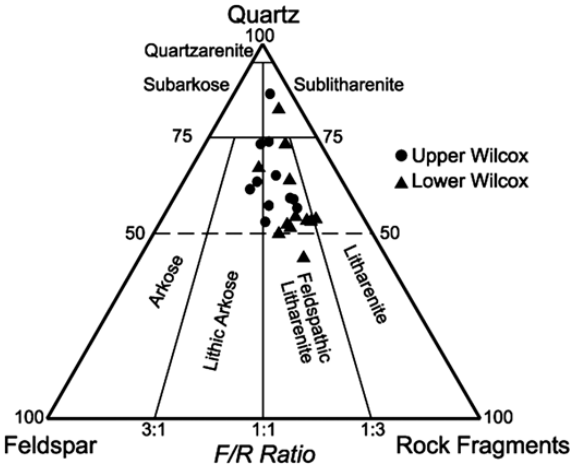


**Figure 3:** Mineralogy of rocks for upper and lower Wilcox (Loucks and Dutton, 2019).

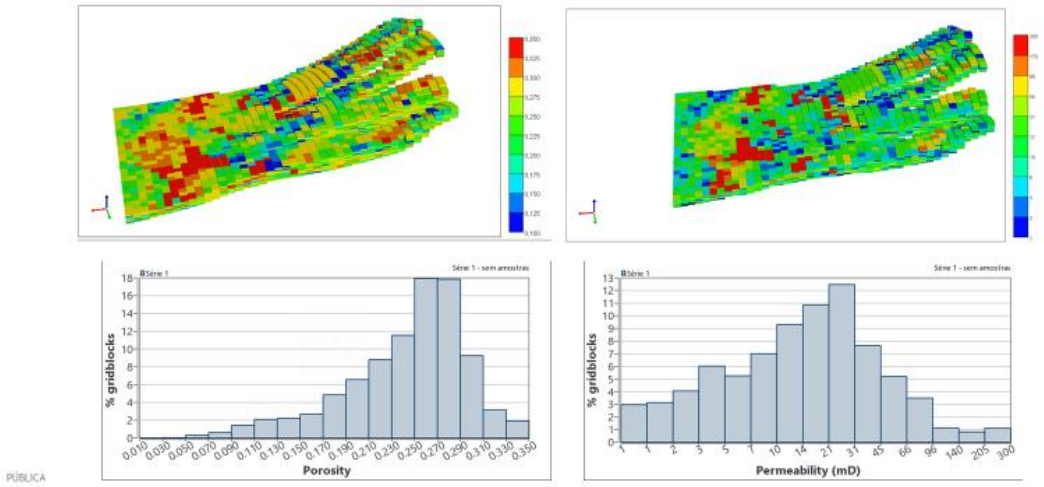


**Figure 4:** Porosity (on left) and permeability (on right) to represent a heterogeneous petrophysical distribution for Wilcox.

## Dynamic non-isothermal characterization

According to Bebout et al. (1982) and Robinson et al. (1986), the following initial conditions represent average values for the Wilcox Formation:

- Initial temperature = 155 ºC (average gradient of 1.5 ºF/100 ft).
- Initial pressure = 45,000 kPa.
- Maximum bottomhole pressure in the wellbore = 64,121 kPa, calculated from the fracture gradient of 0.93 psi/ft from Wilcox.
- Initial brine Salinity = 60,000 ppm (considering a simple brine with NaCl).

These initial conditions will be used to determine the dynamic characterization of fluid and rock thermal properties, which are crucial for conducting a non-isothermal simulation as intended in this study. The thermal parameters for the dry rock were calculated based on initial pressure and temperature, as highlighted in Figure 5, using correlations provided by Butler (1991) and Somerton (1992):

- Rock thermal conductivity: k = 1.8 W/m.K (Butler, 1991).
- Rock heat capacity: C = 930 J/kg.K (Somerton, 1992).

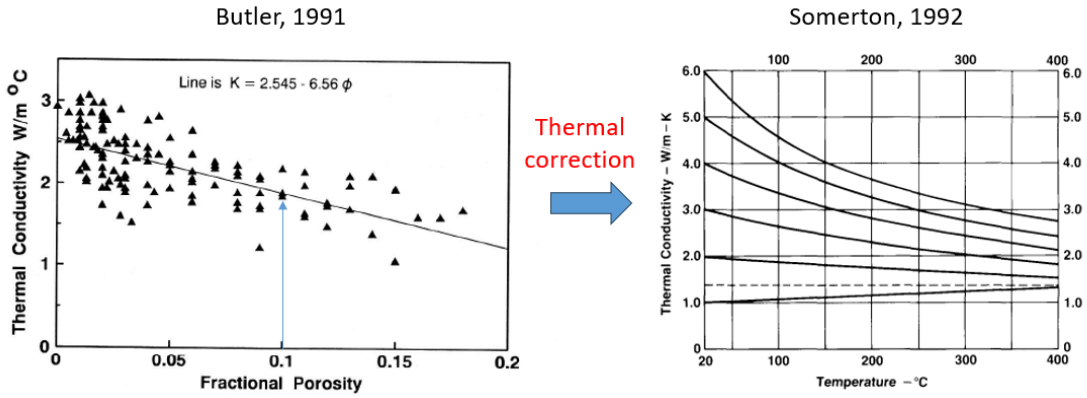


**Figure 5:** Correlation between rock thermal conductivity and fractional porosity. (Butler, 1991) (left) and Thermal conductivity as a function of temperature. (Somerton, 1992) (right)

To characterize the brine, the following properties were calculated using classical and widely validated correlations, based on the parameters they compute. The input for these correlations included initial pressure, temperature, and salinity:

- Brine density: $d_w$ = 0.9793 (Rowe and Chou, 1971).
- Water formation-volume factor: 1.062 (Spivey et al. 2004).
- Brine compressibility: $c_w = 4.56 \times 10^{-5}$ (1/kgf/cm$^2$) (Spivey et al. 2004).
- Brine viscosity: $\mu_w$ = 0.22 cP (Matthews and Russell, 1967).
- Brine thermal conductivity: $k_w$ = 0.856 W/m.K (Cardwell, 1974).
- Brine heat capacity: $C_w$ = 4050 J/kg.K (Sharqawy et al., 2011).

For the $CO_2$ injection case, the properties of $CO_2$ were calculated using the Peng-Robinson Equation of State (PR EoS), and the viscosity was determined using the Jossi-Stiel-Thodos (JST) viscosity model (referenced from Poling et al., 2001). In both water and $CO_2$ flooding scenarios, the heat losses for the overburden, underburden, and lateral boundaries were computed using the analytical method developed by Vinsome and Westerveld (1980). The thermal properties of the rocks, assumed to be shale, were assigned as follows:

- Shale thermal conductivity: k = 1.2 W/m.K (Butler, 1991);
- Shale heat capacity: C = 1012 J/kg.K (Somerton, 1992).

## Well constraints

For the wellbores, whether they are injectors or producers, certain surface constraints were imposed in simulation cases to regulate fluid injections and the heat carried by the produced water. In the case of the injection well, the constraints include:

- Surface temperature: $T_{surf}$ = 30 ºC (according to a geothermal device proposed by Atrens et al., 2009).
- Maximum bottomhole pressure: BHP = 64,121 kPa (in agreement with the Wilcox fracture gradient aforementioned).
- Voidage replacement ratio (injection/production rates): void_ratio = 1.

And for producers:

- Minimum well-head pressure: WHP = 2600 kPa (according to a geothermal device proposed by Atrens et al., 2009).
- Closed-loop water injection: produced water is injected back into the aquifer.

The heat losses within the wellbore for the surrounding formations are calculated using Fontanilla and Aziz's model (1982). We applied this model in wells specifically designed for a geothermal producer well, e.g., without tubing. The model incorporates the following specifications:

- casing radius = 0.14 m.
- wellbore length = 3000.0 m.
- cement thickness = 0.205 m.

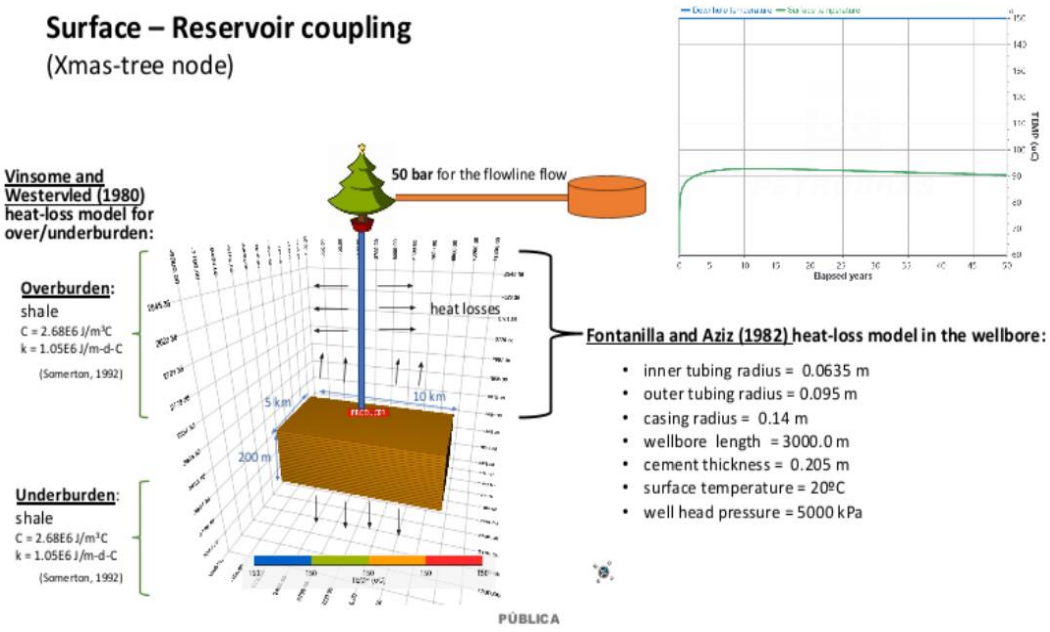


**Figure 6:** Schematic representation of the surface-to-reservoir thermal coupling via the Xmas-tree node, incorporating heat-loss models for the overburden/underburden (Vinsome and Westerveld, 1980) and the wellbore (Fontanilla and Aziz, 1982).

## Sensitivity analysis with a synthetic and homogeneous model

A coupled thermo-fluid modeling of the geothermal reservoir was performed using Computer Modeling Group (CMG) STARS thermal simulator. It is commonly used to devise and develop strategies for geothermal energy recovery. Initially, a simple homogeneous box model was employed with only one standalone producer, as illustrated in Figure 7, to validate the wellbore constraints. The heat losses to the overburden and underburden rocks were also modeled in the reservoir and the wellbore. The input properties are detailed in Table 1.

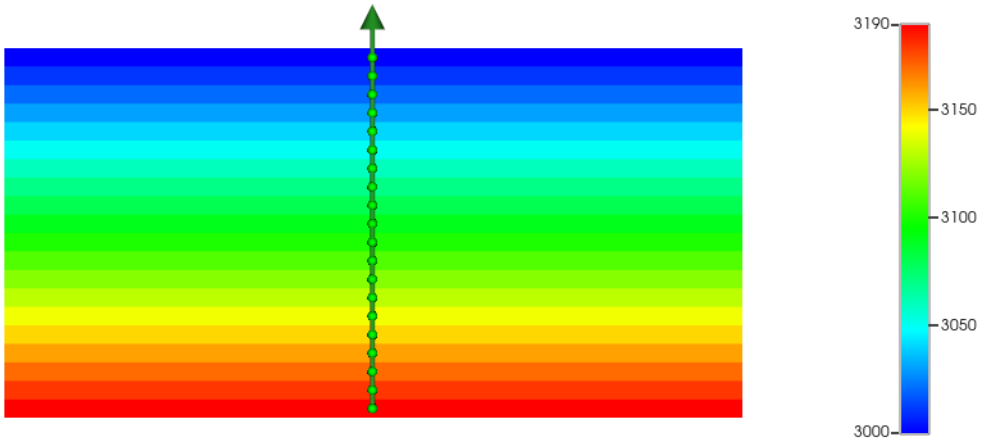


**Figure 7:** 2D view of the model with the producer in the middle highlighting the Grid Top (m).

**Table 1:** – Properties for single wellbore synthetic model.

| **Property** | **Value** |
|---|---|
| Model Dimensions | 10 km x 5 km x 0.2 km |
| Number of Grid-Blocks | 400 x 100 x 20 |
| Depth | 3000 m |
| Porosity | 0.15 |
| Permeability | 10 mD |
| Pressure | 48265 kPa |
| Temperature | 150 ℃ |
| **Producer Constraints:** | |
| Minimum Well-Head Pressure | 5000 kPa |
| Maximum Water Rate | 5000 $m^3$ |

**Case A.1: One water production well.** Figure 8 shows the bottomhole water rate, surface temperature, and bottomhole pressure. The water production rate declines to less than 500 m³/d after 35 years, whereas the surface temperature remains relatively stable, decreasing only by 20 °C to 120 °C.

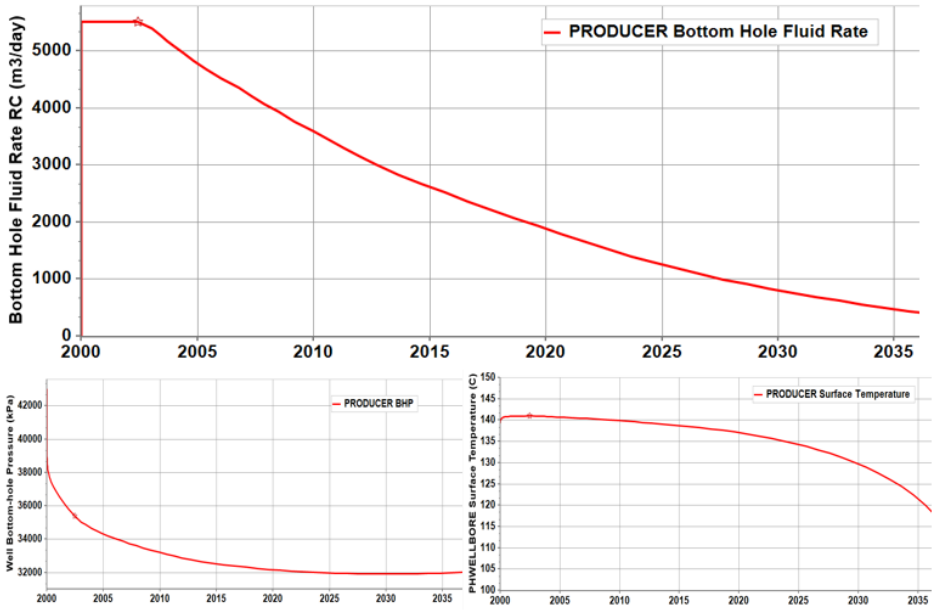


**Figure 8:** Surface water rate (m³/d), bottomhole pressure (kPa), and surface temperature (ºC) for Case A.1.

**Case A.2: Case A.1 with a water injector.** A producer 1000 m from the injection well is modeled to support the production rate. The surface water injection temperature is kept at 30 ºC and is operated at a maximum rate of 5000 $m^3$/day and a maximum BHP of 64,121 kPa. Figures 5 and 6 validate the expected behaviour where a higher water production rate is sustained and the produced water temperature is as high as 140 ºC.

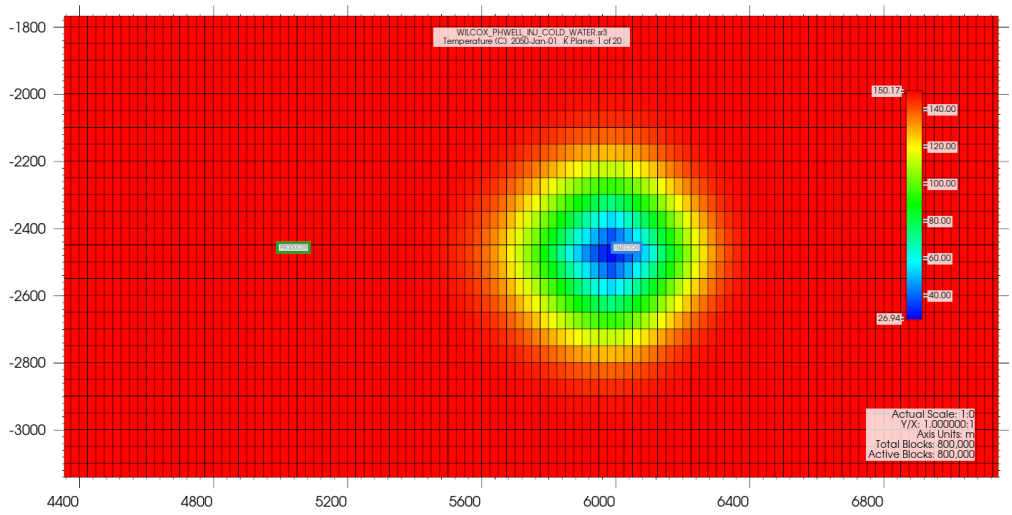


**Figure 9:** Temperature profile (ºC ) in the top layer after 50 years.

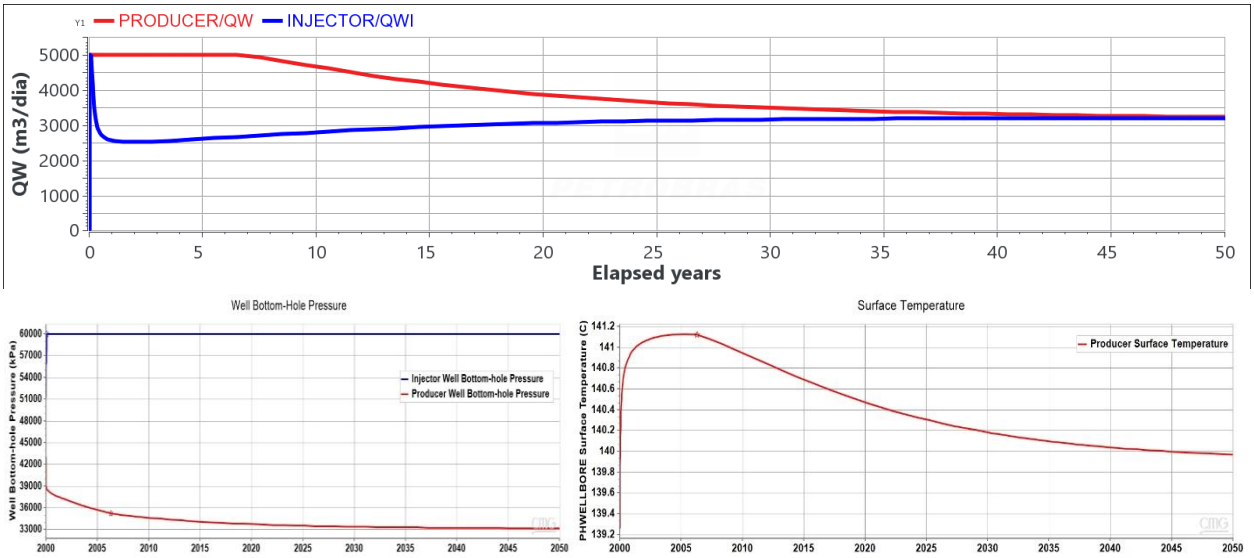


**Figure 10:** Injection and production rates at surface conditions ($m^3/d$), BHP for both wells (kPa), and wellhead temperature (ºC) vs. time.

Figures 11 and 12 compare the results of the above cases and indicate that the water injector support is essential to increase and maintain both bottomhole water rate and temperature.

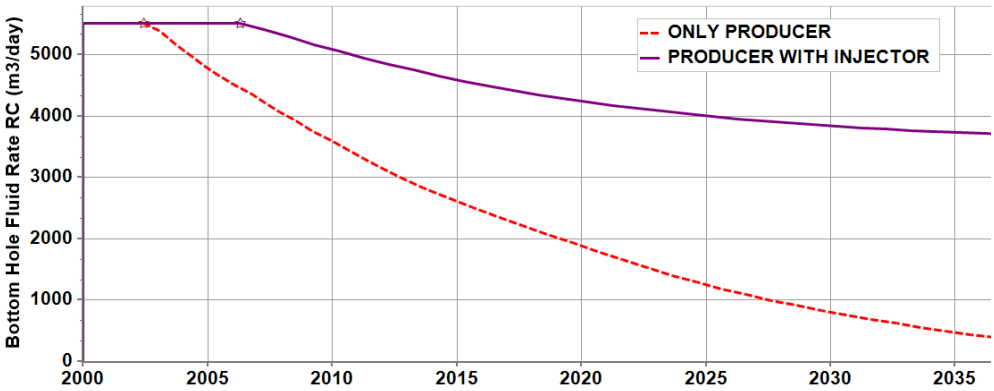


**Figure 11:** Surface produced water rate for 1-well (red) and 2-well (blue) cases indicating a much higher rate when a water injector is added.

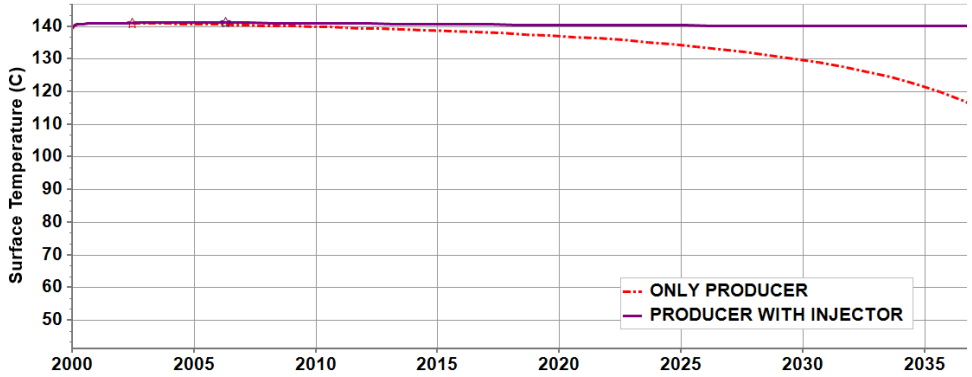


**Figure 12:** The surface temperature for 1-well (red) and 2-well (blue) cases indicates a very stable temperature when a water injector is added.

## Heat recovery with a heterogeneous model

To accurately represent the Wilcox formation, we expanded the model to capture its characteristics in greater detail. The model dimensions are 83 x 62 x 26, resulting in a total of 133,796 grid blocks. Out of these, 117,624 are null blocks, and 16,172 are active. The grids measure 40 meters in both the i and j directions, while the k direction varies but averages approximately 1 meter.

The model includes three major faults that influence reservoir connectivity:

- Sealing faults act as effective barriers, preventing fluid movement between sections.
- The regions where the faults are in contact are transmissible with harmonic averaging used to compute inter-block transmissibility.
- The faults measure approximately 880 meters, 480 meters, and 760 meters, affecting pressure depletion and thermal breakthrough behavior.

To reduce computational complexity while preserving a reservoir representativeness, a sector model was extracted. Unlike the field-scale model, the sector model excludes faults, providing a controlled environment to analyze injections and production dynamics without the influence of structural discontinuities. This approach allows for focused evaluation of thermal dispersion, pressure support, and production sustainability, ensuring that key performance trends are accurately captured.

The sector model serves as a benchmark case for understanding fundamental reservoir behavior, while the full-field model incorporates geological complexities to simulate the Wilcox geothermal production scenarios. Knowledge gained from the sector model is integrated into the full-field model to refine long-term operational strategies.

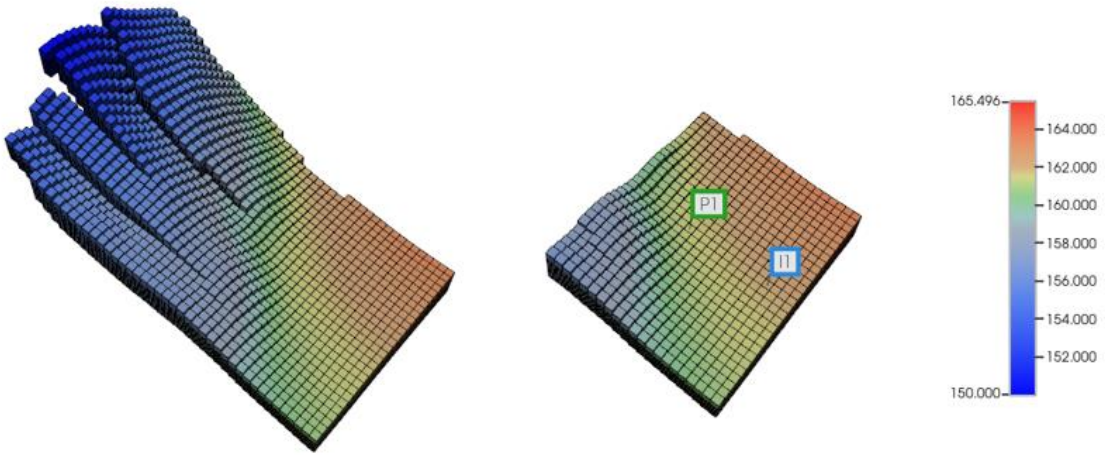


**Figure 13:** Temperature distribution (in $^{o}$C) for full-scale model of Wilcox (left) and sector model (right).

**Sector Model with water injection**

For the sector model, the inter-well distance is set at 400 m. The constraints are set according to Table 2.

Table 2: Sector Model Well Constraints

| **Injection Constraints** | **Producer Constraints** |
|---|---|
| Maximum Bottom-Hole Pressure: 64121 kPa | Minimum Well-Head Pressure: 5000 kPa |
| Maximum Water Injected: 5000 $m^3$/day | Maximum Water Production: 5000 $m^3$/day |

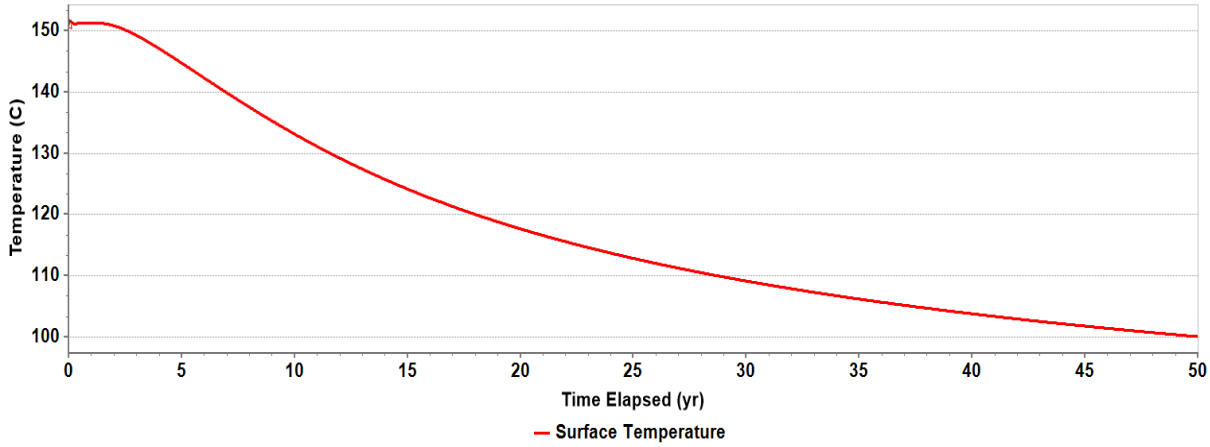


**Figure 14:** Producer temperature versus time elapsed for the sector model with 2-well case.

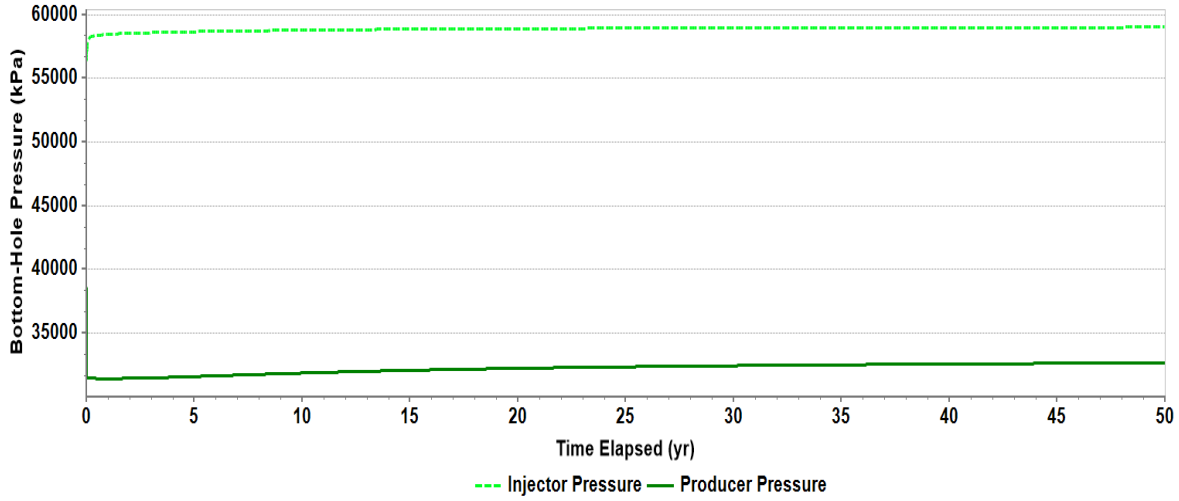


**Figure 15:** Producer and injector bottomhole pressure versus time elapsed for the sector model.

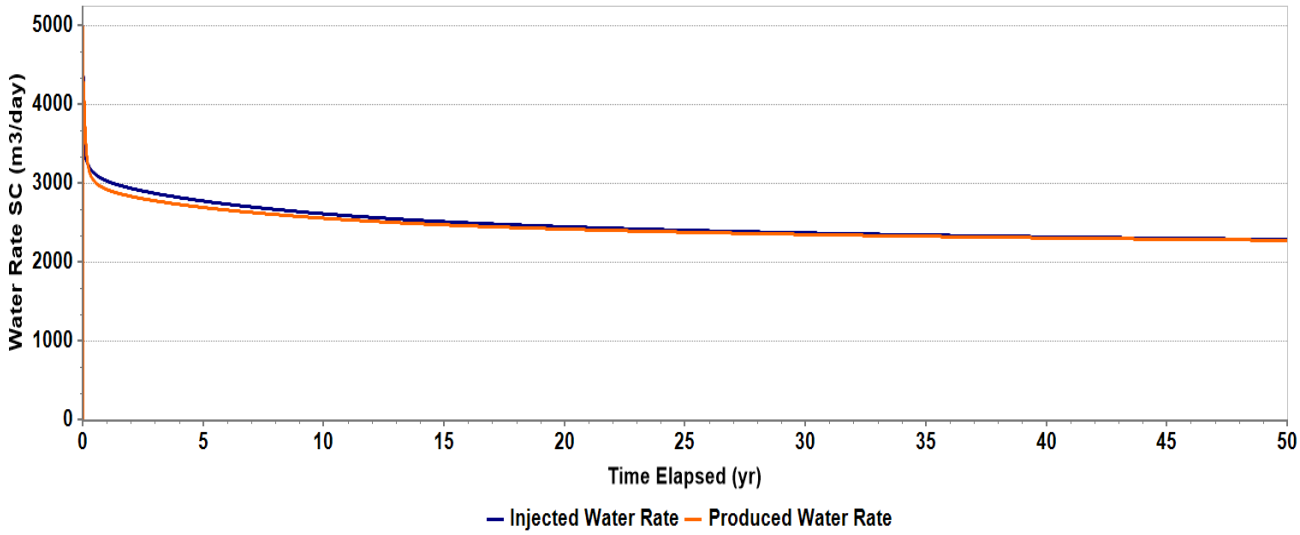


**Figure 16:** Producer and injection bottomhole rates versus time elapsed for the sector model.

Figures 14, 15 and 16 present the production profile for the simulation of a two-well system where water was used as the working fluid. At the start of the simulation, water injection is approximately 3,400 $m^3$/day, which gradually declines to about 2,200 $m^3$/day over the 50-year simulation period. The producer maintains a bottom-hole pressure of around 32000 kPa, while the injector well operates at a higher pressure of about 58,000 kPa. This results in a substantial pressure differential of 26,000 kPa, driving the movement of water from the injector to the producer well.

The temperature profile shows a decline, starting at 150 °C and dropping to about 100 °C, indicating a temperature reduction of 50 °C over the simulation period. This decline in temperature can be reduced by several sensitivity studies.

**Sensitivity Analysis**

**Sensitivity I: Maximum Water injection and production rates**

A sensitivity analysis for maximum water injection was performed by varying the water injection rates between 2500 and 7500 $m^3$/day, while keeping other parameters constant. Since the model initially produced between 3400 and 2200 $m^3$/day, which was below the maximum constraint of 5000 $m^3$/day, the plots for higher injection constraints remained essentially the same. To gain better insight, the model was also run at a lower injection rate of 1500 $m^3$/day.

It was observed that lower injection rates, despite rendering a lower temperature at the beginning of the simulation, led to a less significant temperature drop. At an injection rate of 1500 $m^3$/day, the initial temperature was 146°C, which gradually decreased to 113°C over time—an overall drop of 33°C, which is less sharp compared to the 50°C decline in the base case. However, the rate of water produced was significantly lower. Therefore, a balance must be achieved depending on the surface requirements.

For a two-well model, higher production rates resulted in more heat generation but led to an earlier thermal breakthrough at the production well. Following the thermal breakthrough, the temperature dropped relatively faster due to slow heat conduction in the low-permeable surrounding rock matrix. The changes in sensitivity are illustrated in Figures 17, 18, and 19.

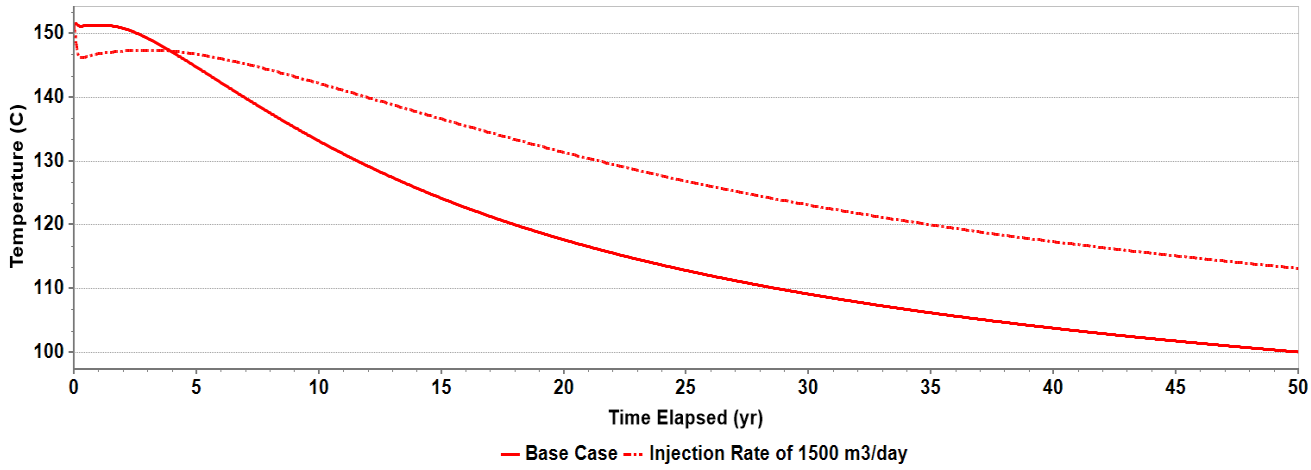


**Figure 17:** Sector model surface temperatures for a lower injection rate compared to the base case.

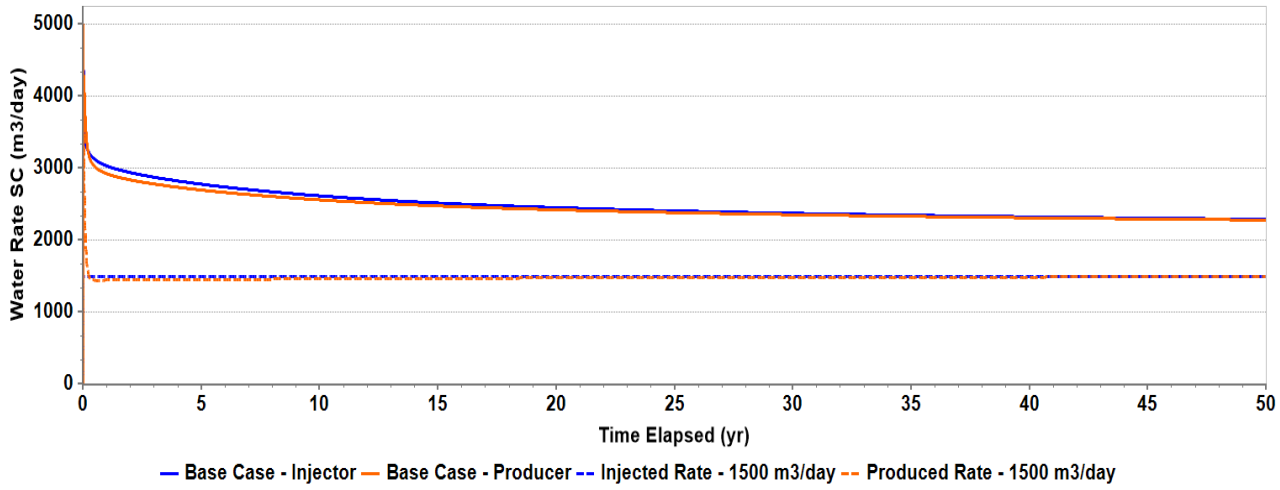


**Figure 18:** Comparison between base case injection and production rates with a lower rate for the sector model as a function of time.

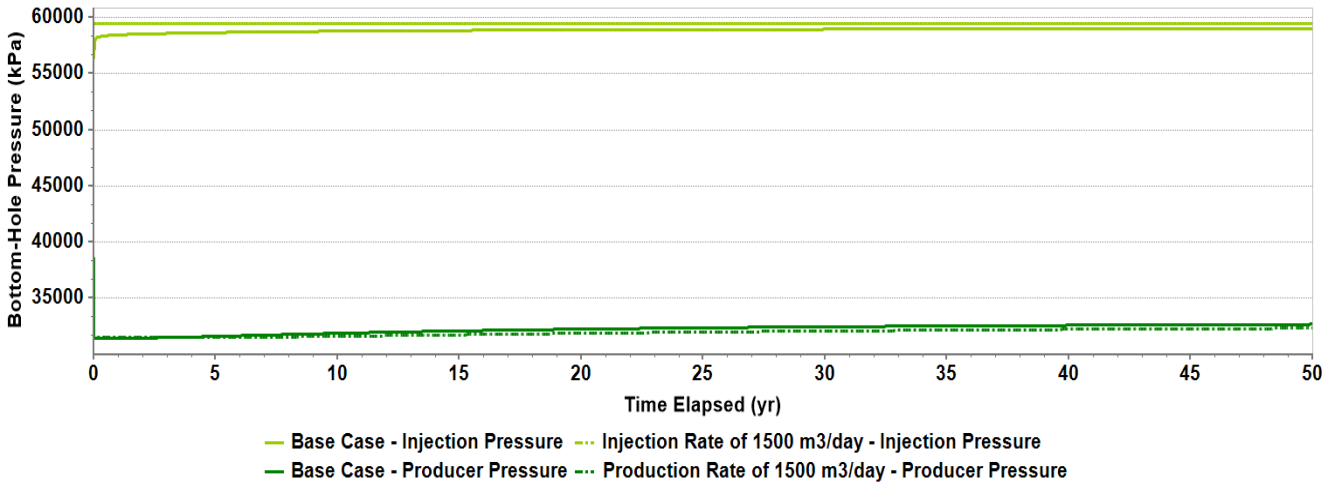


**Figure 19:** Comparison between injection and production pressures of the base case with a lower rate case for the sector model as a function of time.

### Sensitivity II: Tubing Diameters

To evaluate the effect of tubing diameters on the thermal efficiency of a reservoir, sensitivity analyses were performed for four different tubing diameters: 1 inch, 4 inches, 7 5/8 inches, and 20 inches. These variations were applied to both the injector and producer wells, with particular attention to larger tubing sizes, which are more common in geothermal operations compared to conventional oil and gas reservoirs. The inner tubing, outer tubing, and casing sizes remained constant throughout the analysis. Several key observations were revealed. Water production rates were lower for smaller wellbores but increased with tubing size, converging to similar rates beyond a certain diameter (~7 5/8 inches), at which point the curves overlapped. The surface temperature analysis indicated that larger tubing sizes experienced lower temperatures, which dropped sharply and appeared to stabilize over time. Smaller tubing sizes maintained a fairly consistent temperature throughout the simulation. These changes are presented in Figures 20, 21, 22, and 23.

This also leads to the conclusion that larger tubings carry the same amount of liquid, and suffer a higher temperature drop. Therefore, a fair balance between bigger tubing sizes and temperature generation is of paramount significance.

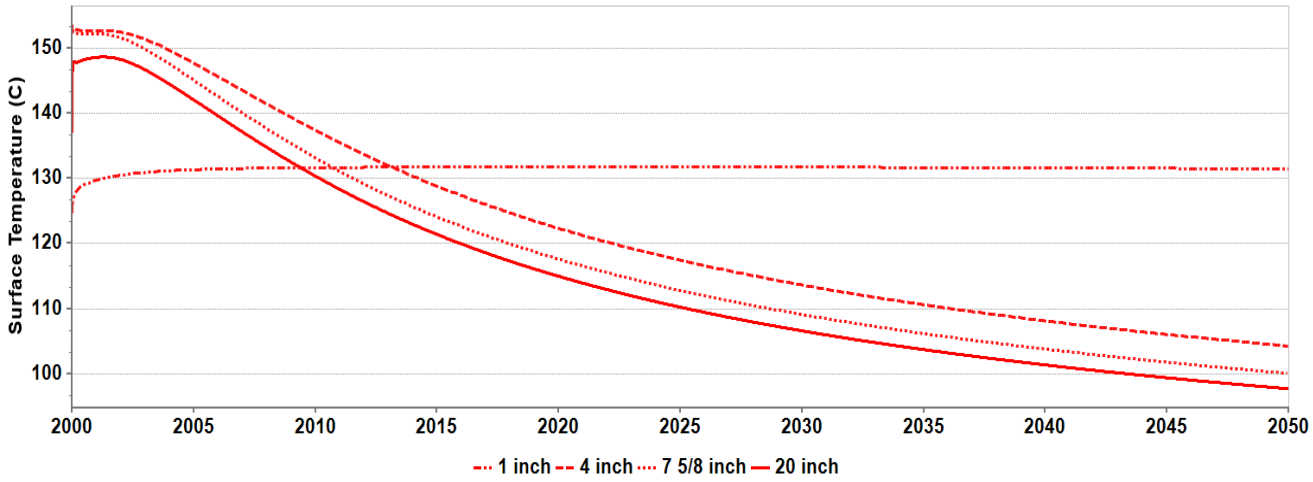


**Figure 20:** Producer temperatures for different tubing sizes.

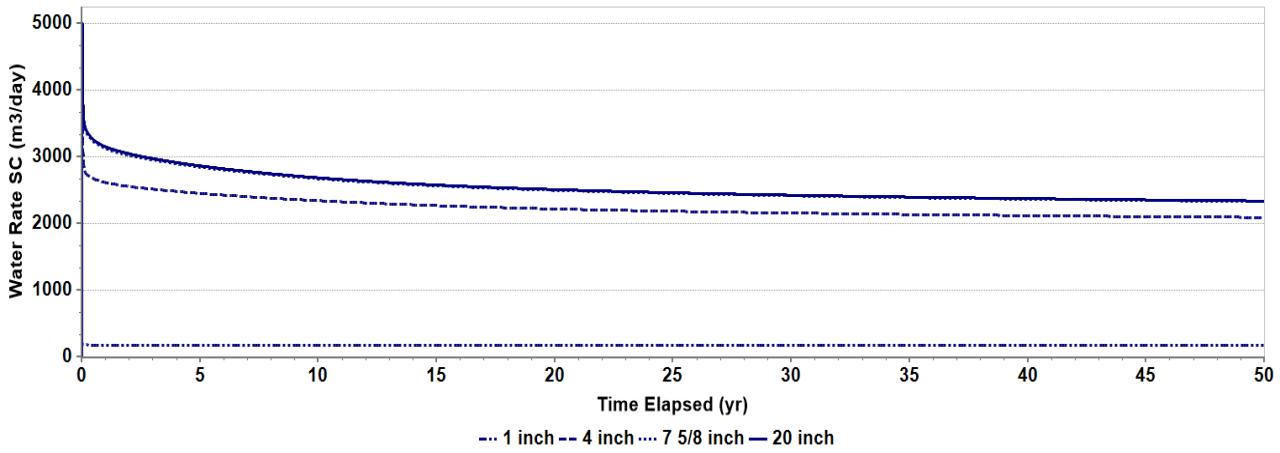


**Figure 21:** Water production rates for different tubing sizes.

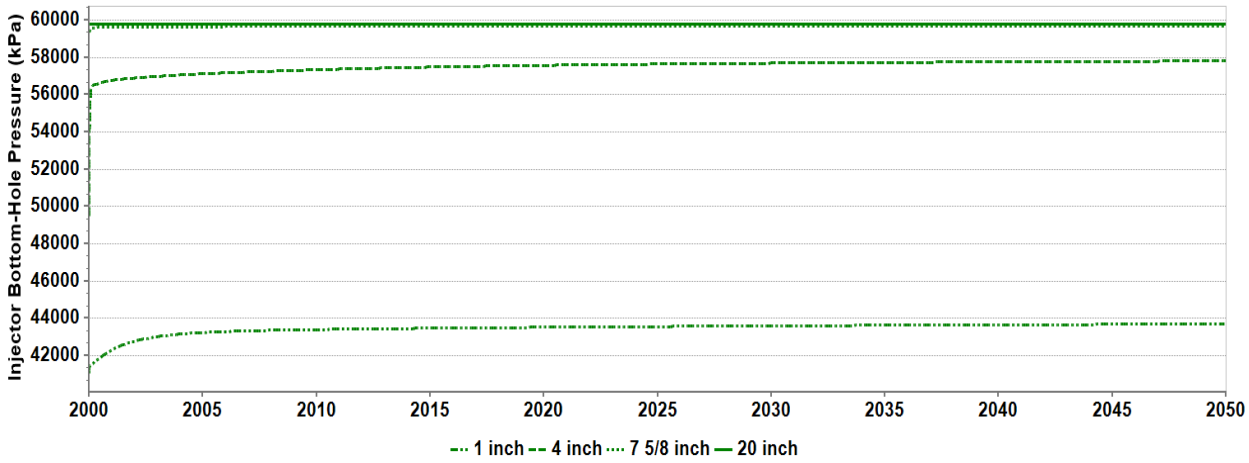


**Figure 22:** Injector bottomhole pressure for different tubing sizes.

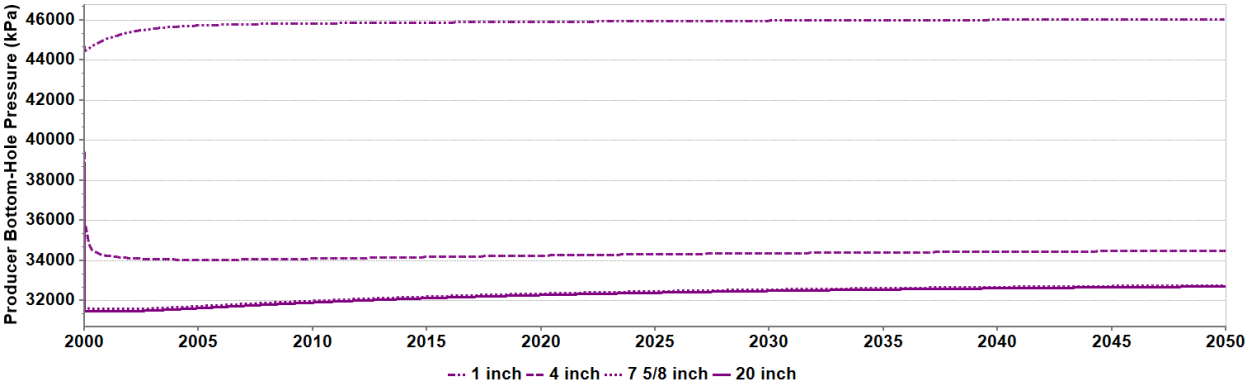


**Figure 23:** Producer bottomhole pressure for different tubing sizes.

### Sensitivity III: Inter-Well Distance

Three different well spacing configurations were tested to analyse the impact of well spacing: 200 meters, 400 meters, and 600 meters. The analysis reveals shorter well spacing leads to a more rapid temperature decline at the producer well. At 200 meters, the produced fluid temperature drops quickly, reaching 80 °C after 50 years. At 400 meters, the temperature decline is more moderate, stabilizing around 100 °C. The largest spacing of 600 meters exhibits the slowest decline, with temperatures stabilizing at approximately 120 °C.

Well spacing also significantly impacts water production rates. The shortest spacing (200 meters) starts with the lowest rates, gradually declining to less than 2000 $m^3$/day over the simulation period. In contrast, at 600 meters, the system begins with the highest flow rates (~3600 $m^3$/day), gradually declining to ~2600 $m^3$/day over 50 years.

The injection well pressures remain consistent across all cases, starting between 54,000 and 55,000 kPa, as injection constraints were kept the same. However, the producer well pressures exhibit notable differences. The shortest inter-well distance (200 meters) results in the highest producer bottom-hole pressures, primarily due to earlier thermal breakthrough and reduced drawdown efficiency. In contrast, at 600 meters, producer well pressures are lower, reflecting a more gradual and stable reservoir depletion process. This trend is revealed in Figures 24, 25 and 26.

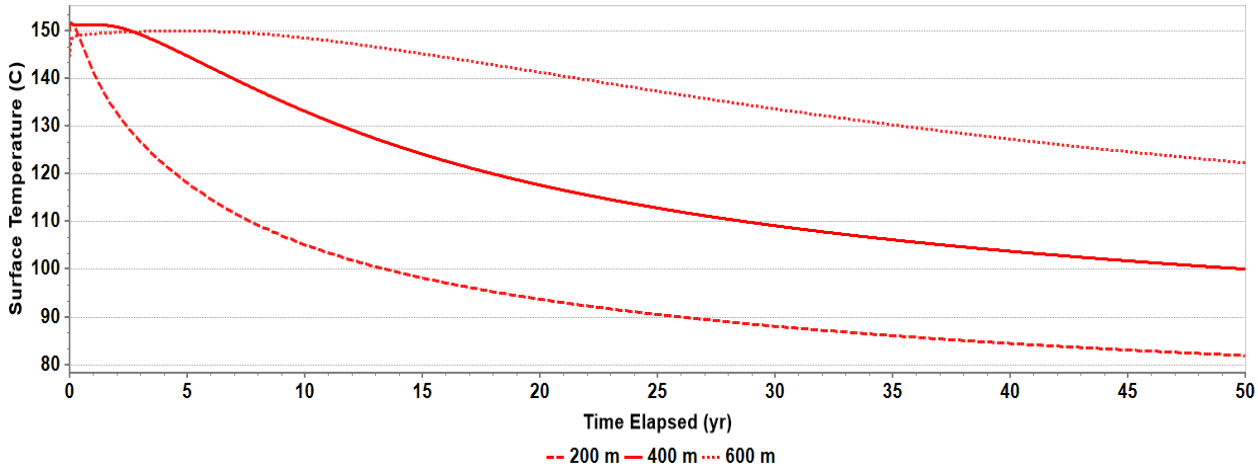


**Figure 24:** Producer surface temperature as a function of inter-well distance.

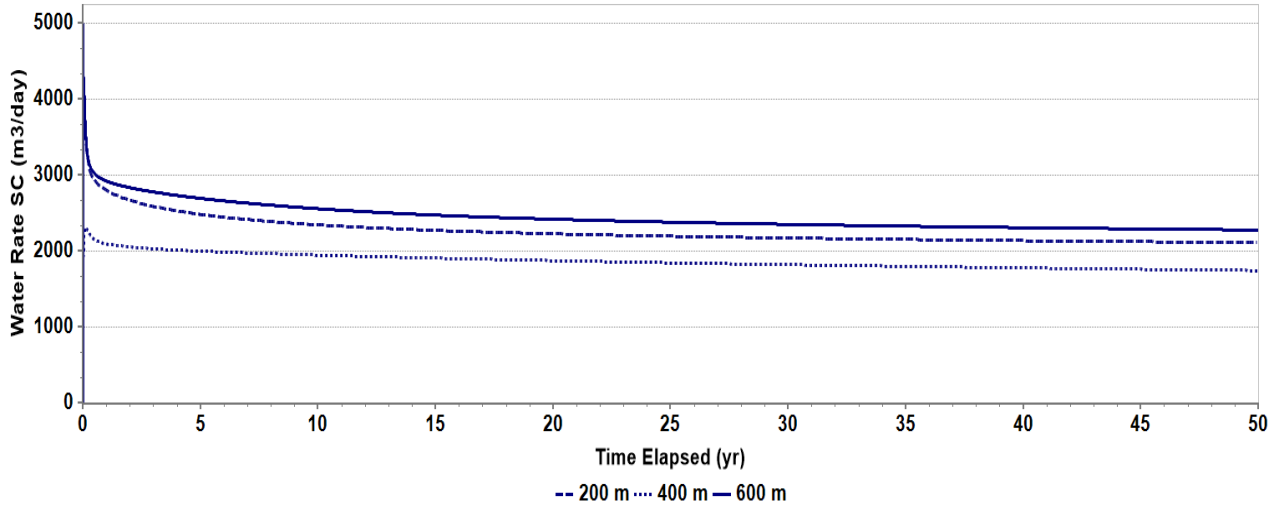


**Figure 25:** Producer rate as a function of inter-well distance.

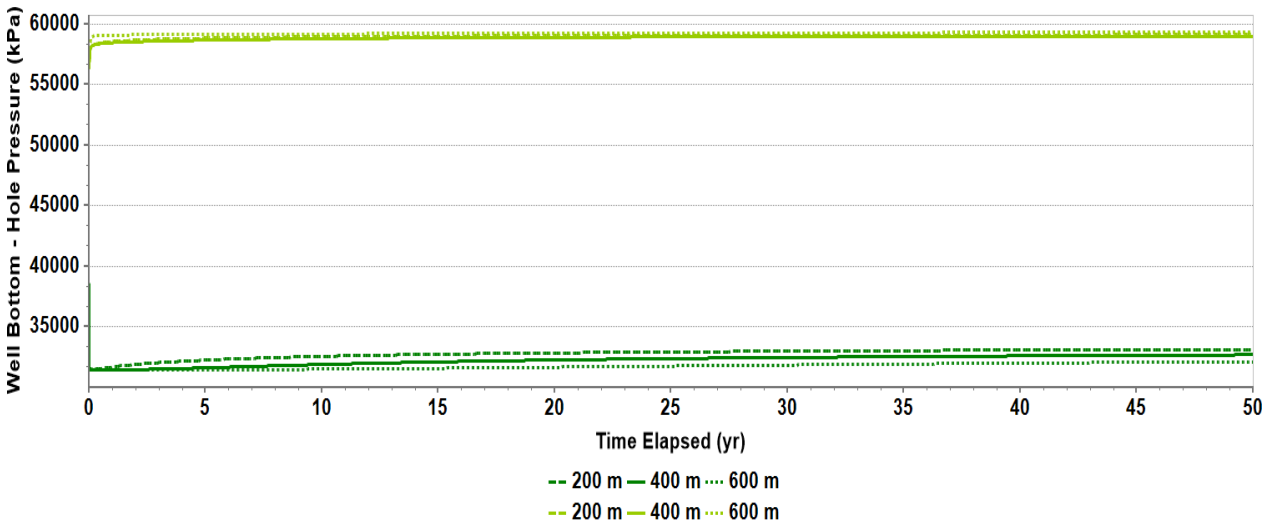


**Figure 26:** Producer and injector bottomhole pressures as a function of inter-well distance.

### Entire Model along with the faults

Further simulations of water as a heat-carrier fluid were performed on the entire model with two wells. The model that consists of the heterogeneities is shown in Figure 27. The same constraints are applied as the sector model.

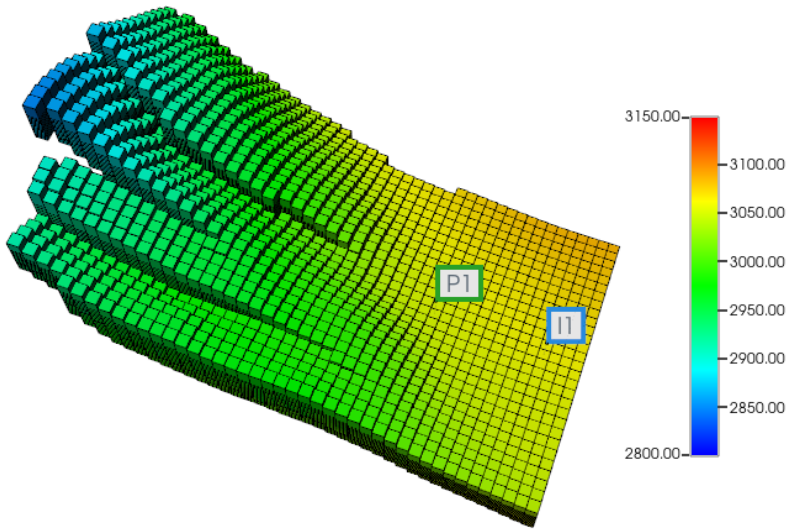


**Figure 27:** 3D view of the model with the dip including the positions of the injector and producer. The color scale shows grid top depth in m.

For the production profile (Figures 28, 29 and 30), the pattern for the full model follows the same trend as the sector model. The temperature decreases from 150 °C to 100 °C while maintaining relatively constant pressure rates and same injection and production rates.

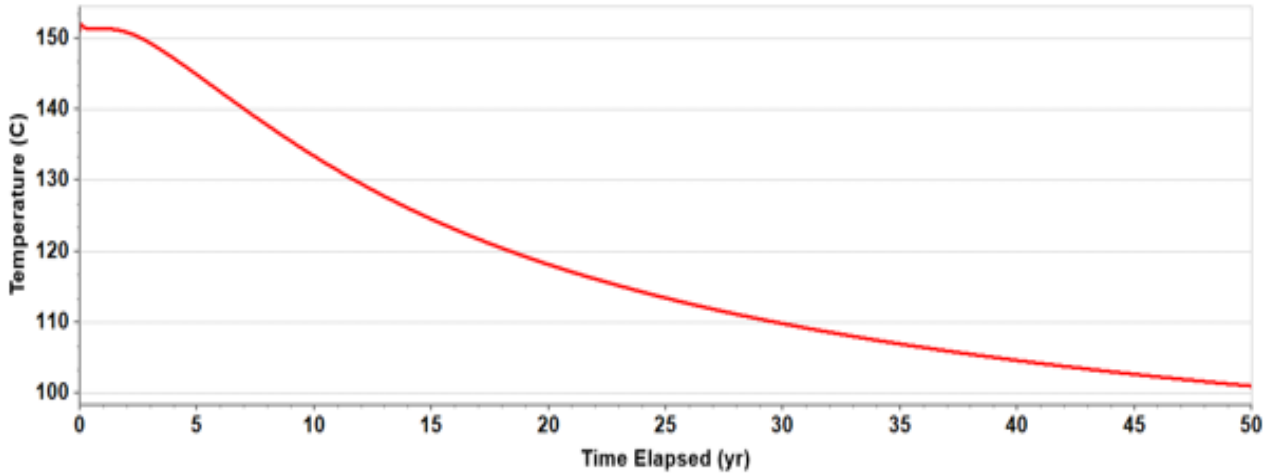


**Figure 28:** Temperature Distribution for the complete model with elapsed time

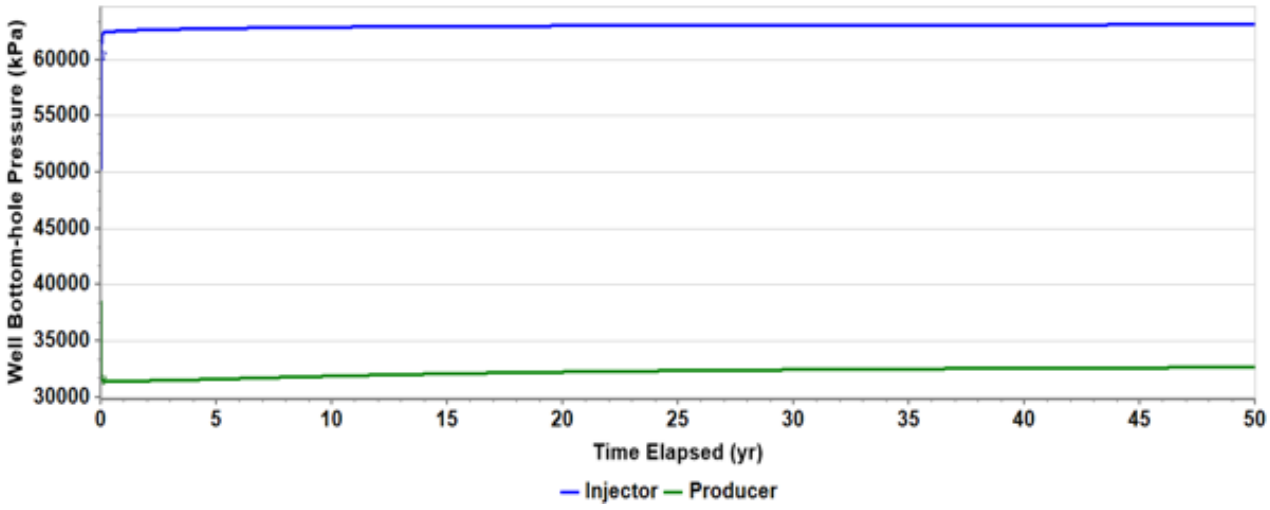


**Figure 29:** Well bottomhole pressure profile for the full- model with elapsed time.

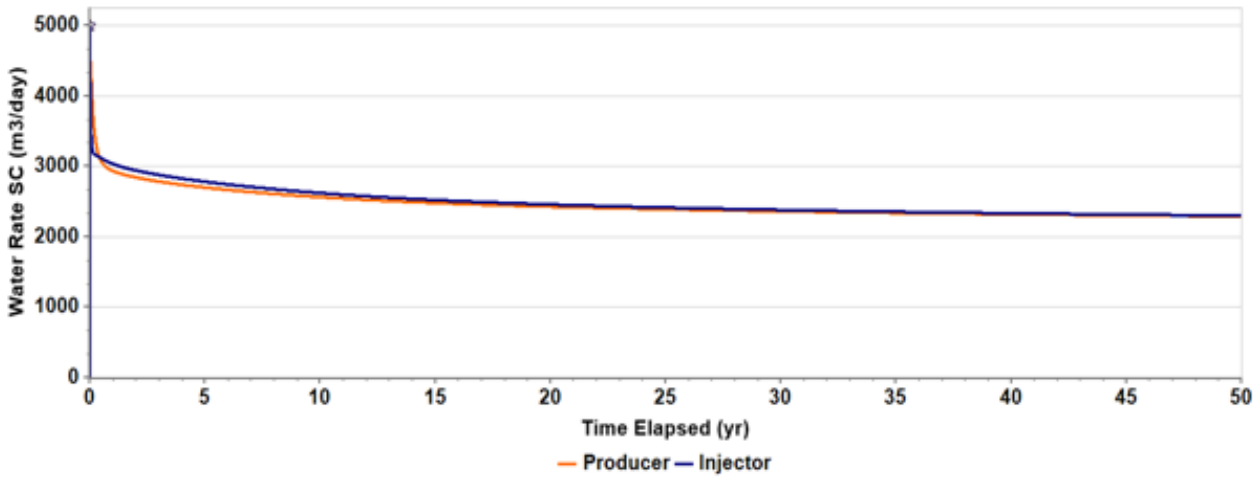


**Figure 30:** Water rates for the full model with elapsed time.

The interaction between water injection rates and residence time, which is influenced by the distance between the wells, plays a critical role in controlling the reservoir's temperature. In order to understand this effect and the impact of the well distances, we devised three cases as shown in Figure 31.

- The first case, CASE A is the base case of the model which we have discussed already.
- In CASE B, we have kept the producer at the same position, while moving the producer up the slope.
- In CASE C, we have interchanged the positions of the injector and producer from the CASE B.

The distance between the injector and producer is 400m for CASE A. For CASE B and CASE C it is approximately 1400m.

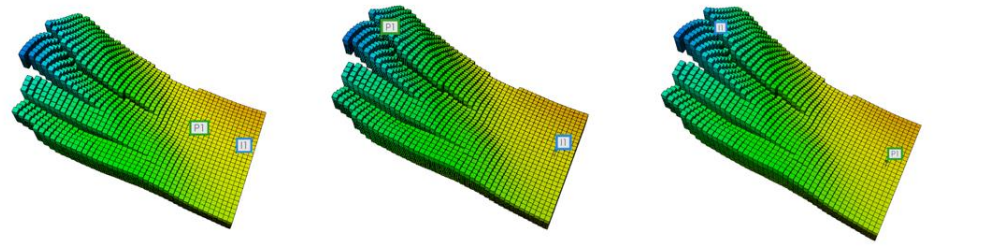


**Figure 31:** Well positions for the study

The reservoir simulation yields several significant conclusions, with well placement emerging as a critical factor influencing production rates and temperatures. The placement of wells should be determined based on the reservoir's temperature profile and gradient, which varies from 150°C to 163°C in the model.

The evolution of reservoir temperature is affected by the movement of injected water and the formation's ability to transfer heat over time. Temperature distribution around the wells, illustrated in Figures 32, 33, and 34, demonstrates how cooler injected water spreads and interacts with the surrounding rock before reaching the producer. Over the 50-year simulation period, a substantial temperature decline is observed at the production well in all three cases, but at differing rates.

Case A, with the shortest inter-well distance, experiences the fastest temperature drop, reaching 100°C by the simulation's end. In Case B, where the producer well is situated further up the slope, the temperature decline is more gradual, stabilizing around 120°C. Case C, featuring the injector positioned higher than the producer, maintains the highest produced temperatures, remaining close to 140°C after 50 years. The slower thermal decline in Case C suggests that the injected water has a longer residence time, allowing for better heat transfer before reaching the production well.

Production and injection rates also vary across the three cases, reflecting the differences in well spacing and flow behavior. Figure 33 indicates that Case A consistently achieves the highest production rates, followed by Case B, while Case C yields the lowest. After 50 years, Case A reaches a production rate of approximately 2000 $m^3$/day, benefiting from the large pressure gradient and shorter flow path. Case B, with increased well spacing, achieves a slightly lower production rate of 1800 $m^3$/day, while Case C produces about 1650 $m^3$/day.

A trade-off exists between production rate and thermal efficiency regarding injector and producer rates. While closer well spacing leads to higher flow rates, it also accelerates thermal depletion, ultimately reducing the system's longevity. Conversely, increasing the distance between wells improves temperature sustainability but introduces additional resistance to flow, resulting in lower production rates.

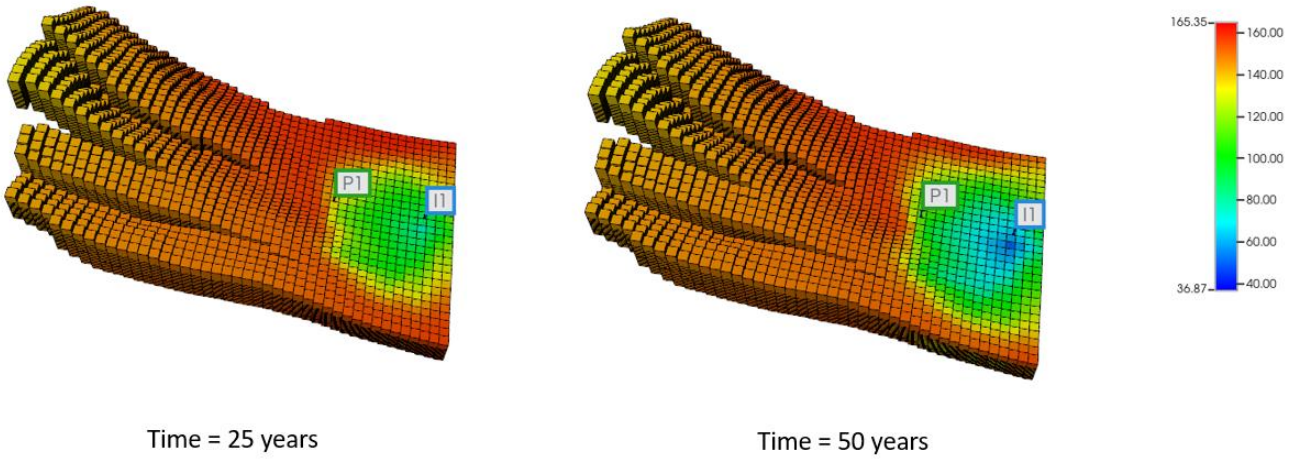


**Figure 32:** Case A - reservoir temperature (in °C) distribution at 25 and 50 years.

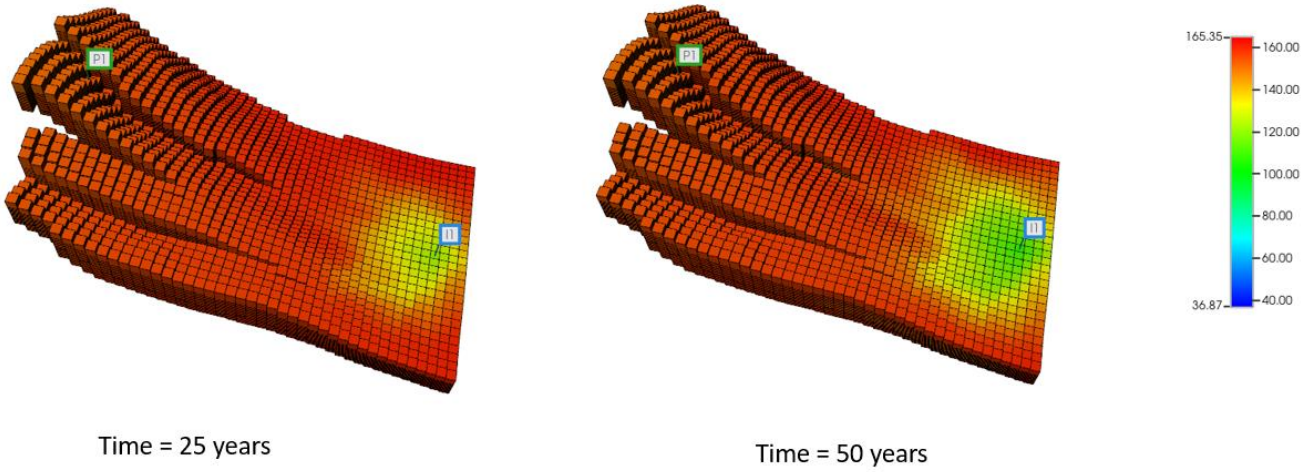


**Figure 33:** Case B - reservoir temperature (in °C) distribution at 25 and 50 years.

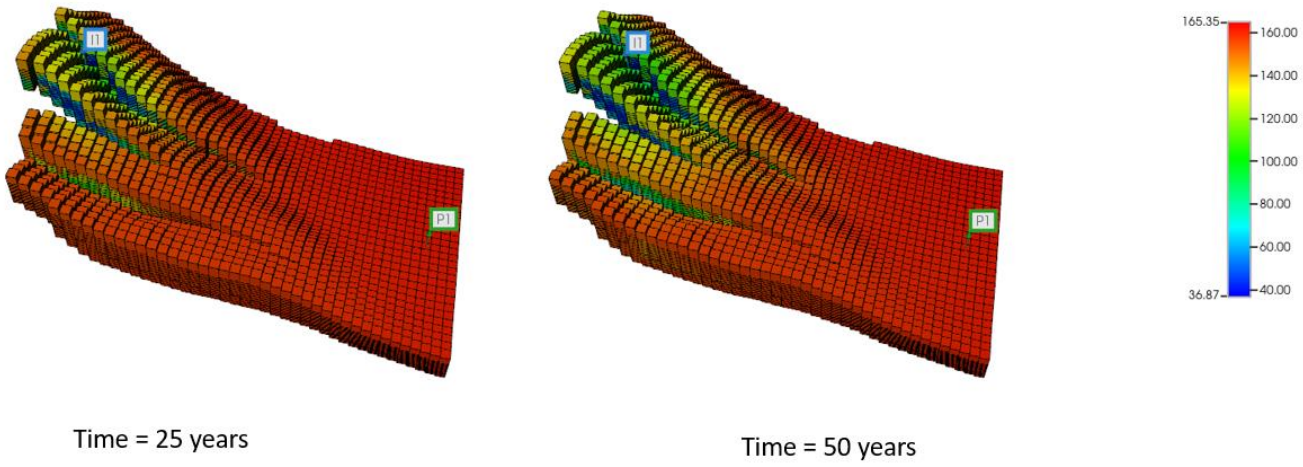


**Figure 34:** Case C - reservoir temperature (in °C) distribution at 25 and 50 years.

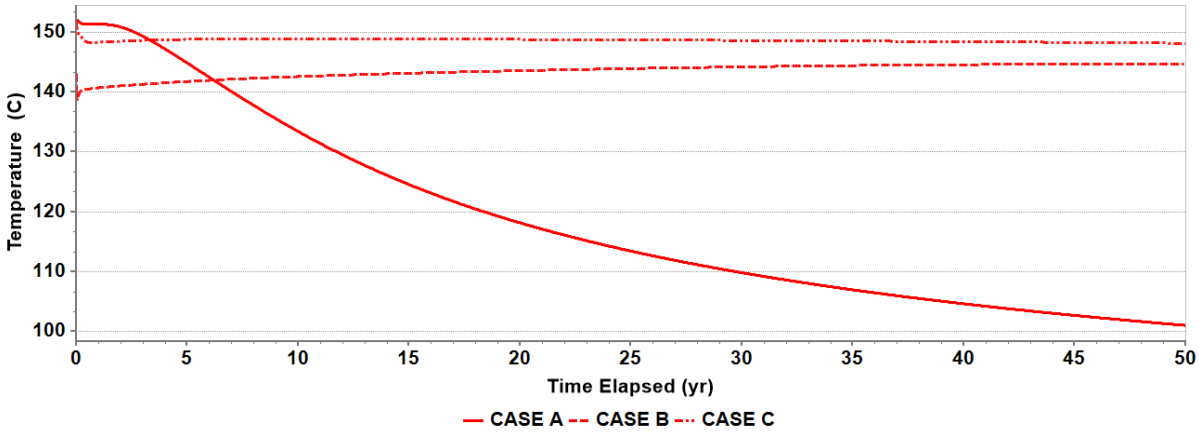


**Figure 35:** Surface temperatures for the producer for different well placement cases.

### Sector Model with $CO_2$ injection

Reservoir modeling studies were undertaken to study the effects of $CO_2$ injection using the sector model. The inter-well distance was kept at 400 m. The constraints set on the producer and injector are highlighted in Table 3.

**Table 3:** $CO_2$ injection Constraints

| Injection Constraints | Producer Constraints |
|---|---|
| Maximum Bottom-Hole Pressure: 64121 kPa | Minimum Well-Head Pressure: 5000 kPa |
| Maximum Injected $CO_2$: 250,000 $m^3$/day | Maximum Water Production: 500 m3/day<br>Gas-Liquid Ratio: 1000 |

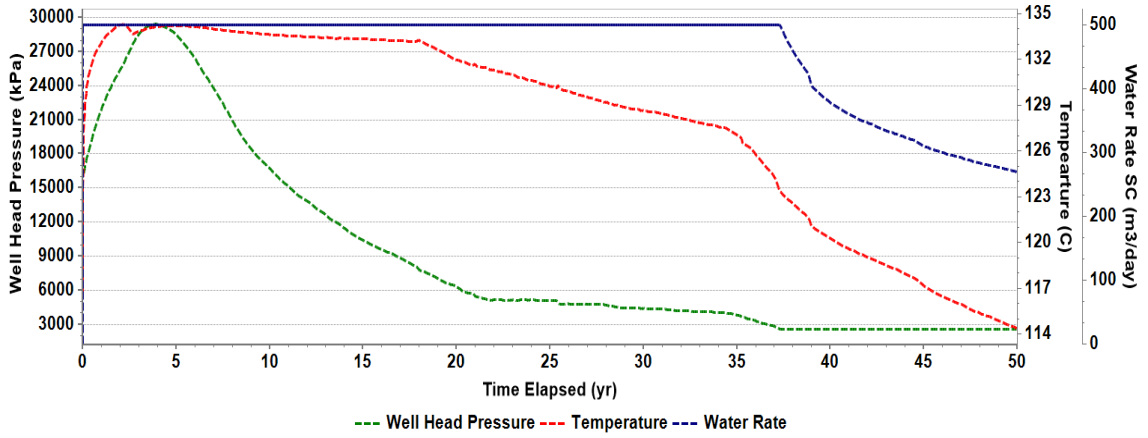


**Figure 36:** Simulation results of the producer well (well-head pressure, temperature, produced water rate) with respect to time.

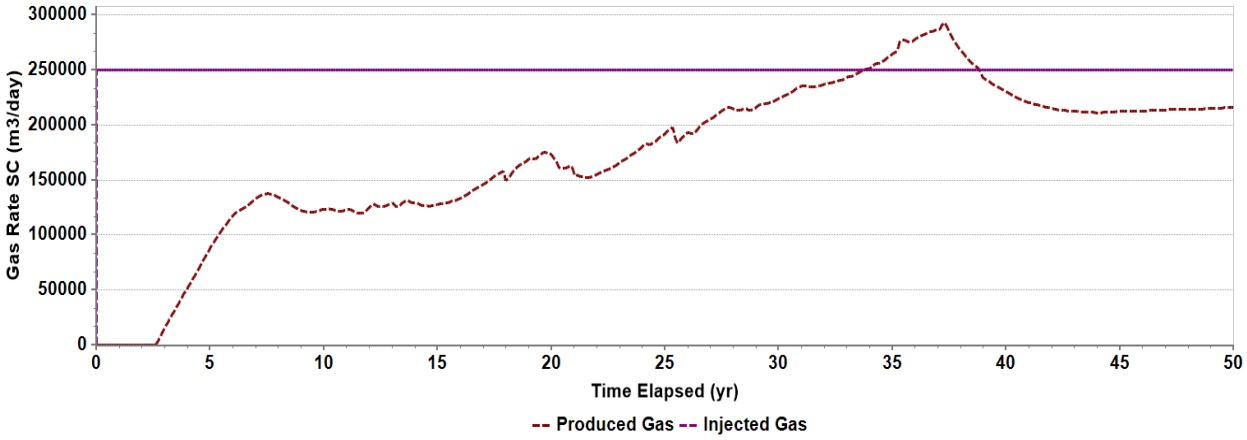


**Figure 37:** Produced and injected $CO_2$ rates with respect to time.

During the initial phase of $CO_2$ injection, the well head pressure exhibited a significant surge, which was due to the $CO_2$ injection into the reservoir. This increase in the well-head pressure

was constant until the breakthrough of $CO_2$ at the production well, which was observed approximately three years into the simulation. Post-breakthrough, a decline in reservoir pressure was recorded, which is attributed to the continuous production of $CO_2$ and water from the model.

The reservoir pressure continues to decrease, approaching the minimum well head pressure constraint at approximately 37 years in the simulation. Once this constraint was reached, a corresponding decline in the water production rate was noted which maintained the minimum well head pressure. This decline in water production rate had a direct impact on the temperature of the produced fluids. It can be observed that the temperature starts declining steeply as soon as the water rate declines.

At the beginning of the simulation, the well head temperature was approximately 134 °C. This temperature began to decrease concurrently with the onset of $CO_2$ production. The temperature of the produced fluids declined sharply when the water production rate started to fall. This indicates that maintaining at least a certain minimum water production rate is essential for sustaining the production of warmer fluid from the reservoir. Over a 50-year simulation period, the reservoir temperature exhibited a gradual decline, reaching approximately 114 °C, which corresponds to a 20 °C decrease from the initial temperature.

Figure 38 illustrates the evolution of temperature, $CO_2$ gas saturation, and $CO_2$ molar fraction within the model over a 50-year simulation period. The figure provides an overview at four key intervals: at the start (0 years), after 20 years, 40 years, and at the end of simulation (EOS). The reservoir temperature initially is as per the geothermal gradient. By 20 years, a cooler spot is prevalent around the injector, which gradually picks up heat from the surrounding reservoir as the injected gas moves towards the producer. At 40 years, the cooler region expands but continues to be warmed by adjacent hotter zones in the reservoir. By the end of the simulation, the temperature around the wellbore has decreased.

The $CO_2$ gas saturation by 20 years of time starts forming a distinct plume. This plume expands towards the producer at 40 years. At the end of the simulation, the $CO_2$ plume has spread extensively in the sector model. This trend is corroborated by the $CO_2$ molar fraction distribution. The $CO_2$ molar fraction increases around the injector and spreads towards the producer over time.

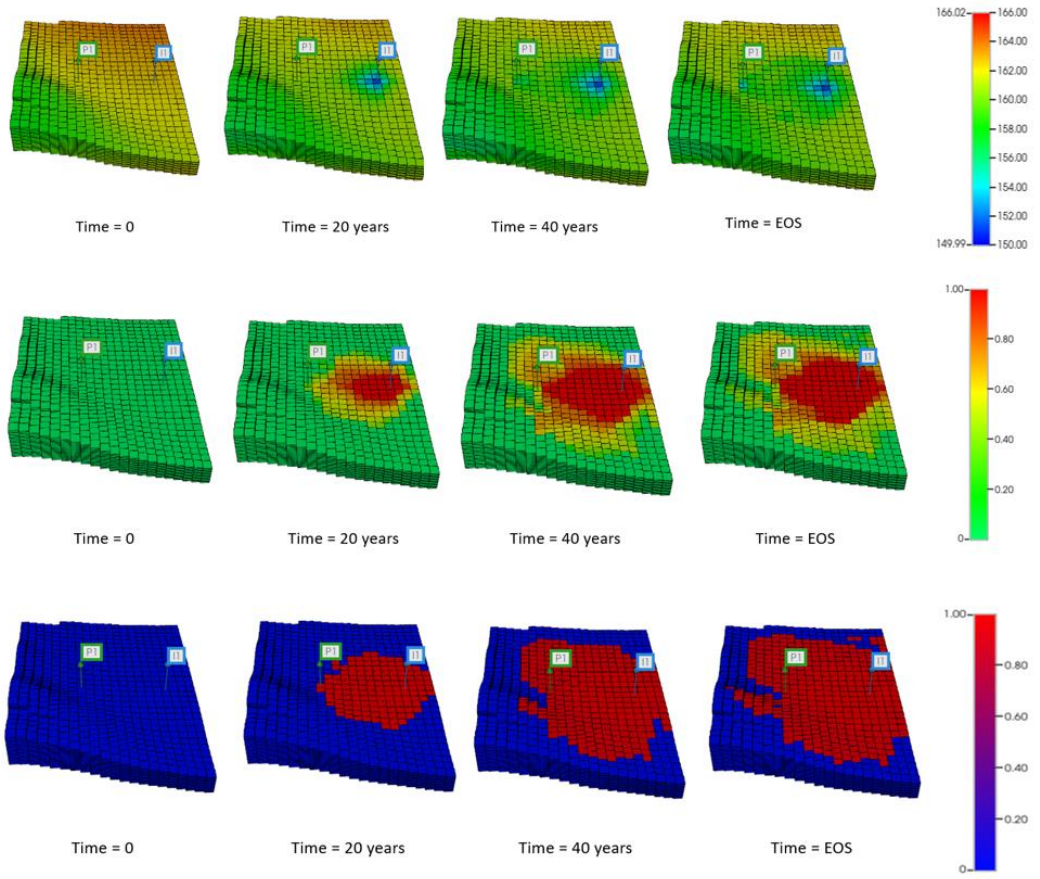


**Figure 38:** Aerial view of the sector model showing the effect of the injection of $CO_2$ on temperature (top), gas saturation (middle), gas mole fraction (bottom).

To validate the model accuracy, the pressure-temperature (P-T) properties were compared with NIST data. Three random grid blocks were selected at random simulation times and compared against NIST values. The gas mass densities and viscosities were found to be consistent with NIST data, indicating that the models accurately represent $CO_2$ in the supercritical state. This becomes important for further modeling of various mechanisms, potentially enabling a combination of carbon capture and storage (CCS) with geothermal projects.

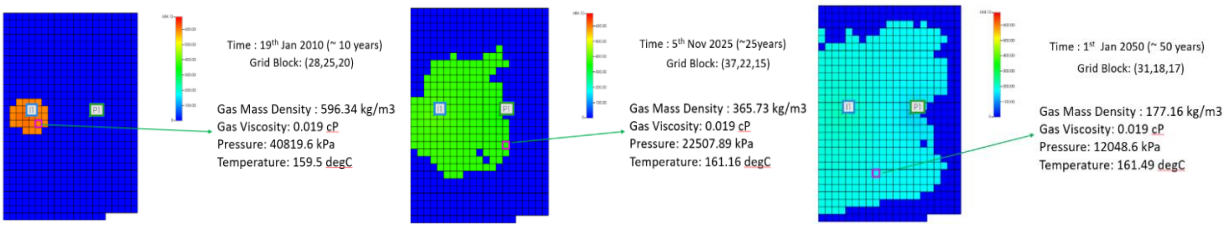


**Isothermal Data for T = 160.00 C**

| Temperature (C) | Pressure (MPa) | Density (kg/m3) | Volume (m3/kg) | Internal Energy (kJ/mol) | Enthalpy (kJ/mol) | Entropy (J/mol*K) | Cv (J/mol*K) | Cp (J/mol*K) | Sound Spd. (m/s) | Joule-Thomson (K/MPa) | Viscosity (cP) | Therm. Cond. (W/m*K) | Phase |
|---|---|---|---|---|---|---|---|---|---|---|---|---|---|
| 160.00 | 10.000 | 139.92 | 0.0071468 | 22.572 | 25.718 | 93.744 | 36.586 | 54.167 | 305.96 | 3.7993 | 0.023472 | 0.033137 | supercritical |
| 160.00 | 20.000 | 309.60 | 0.0032300 | 20.887 | 23.730 | 84.369 | 38.545 | 68.933 | 321.80 | 2.6246 | 0.029252 | 0.043515 | supercritical |
| 160.00 | 30.000 | 466.85 | 0.0021420 | 19.423 | 22.251 | 78.321 | 39.411 | 75.656 | 374.96 | 1.5039 | 0.038455 | 0.056059 | supercritical |
| 160.00 | 40.000 | 581.81 | 0.0017188 | 18.369 | 21.394 | 74.410 | 39.684 | 74.898 | 444.18 | 0.82902 | 0.048200 | 0.066920 | supercritical |
| 160.00 | 50.000 | 663.37 | 0.0015075 | 17.614 | 20.931 | 71.713 | 39.846 | 72.781 | 512.04 | 0.45827 | 0.057055 | 0.075904 | supercritical |
| 160.00 | 60.000 | 724.45 | 0.0013804 | 17.042 | 20.687 | 69.687 | 40.006 | 70.890 | 574.43 | 0.23791 | 0.064980 | 0.083634 | supercritical |

**Figure 39:** Validation of $CO_2$ properties in CMG during simulation using NIST Data.

## Sensitivity Analysis

Based on the constraints, we performed a few sensitivities to understand the impact on the model:

### Sensitivity I: Maximum Water Produced

The initial model produced a specific amount of water, and an analysis was conducted to understand the impact of varying production rates. A decreased production rate of 250 $m^3$/day was compared with the base case of 500 $m^3$/day. It was observed that a lower water production rate resulted in reduced $CO_2$ injection into the reservoir and consequently, less $CO_2$ being produced over the same period. This decrease in production rates led to a correspondingly smaller drop in the produced well-head pressures.

At a lower production rate of 250 $m^3$/day, the well-head pressure dropped to a minimum of 20,000 kPa during the simulation, whereas in the base case, the well-head pressure constraint was reached, followed by a decline in water production. The peak gas production occurred later in scenarios with higher water production and was observed to be higher compared to lower production rates.

For geothermal projects, the most significant change was in temperature. Lower surface temperatures were maintained below 120 °C throughout the simulation when less water was produced. These variations are illustrated in Figure 40.

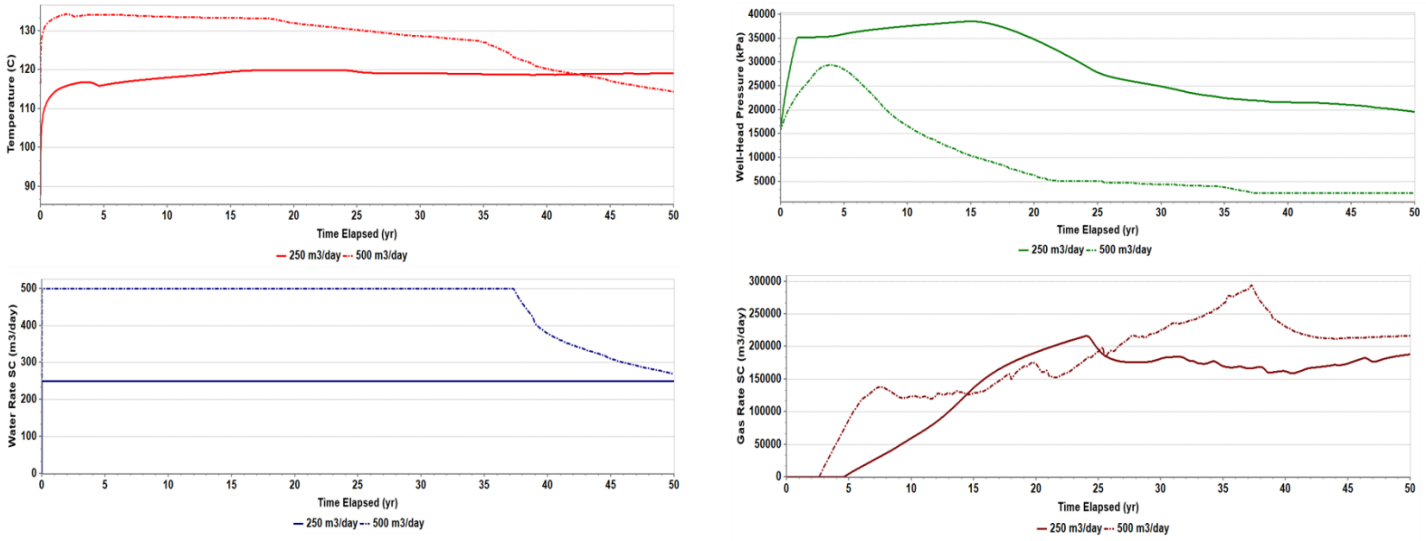


**Figure 40:** Comparison of decreased water production rate through Surface Temperature (top left), well-head pressure (top right), water rate (bottom left) and gas rate (bottom right).

### Sensitivity II: Maximum $CO_2$ injected

A GLR constraint of 1000 was established to limit the amount of gas produced in order to generate heat more effectively. Once the constraint is reached, the producer well is shut in. Figure 15 illustrates the sensitivity results as a function of CO2 injected. Injection of CO2 increases the pressure, meaning more CO2 injection results in higher pressure. Higher CO2 production leads to higher temperatures. However, increased CO2 injection causes the GLR constraint to be met, subsequently halting the simulation at that point.

At higher injection rates and elevated GLR levels, numerical issues were observed. Specifically, injecting 500,000 $m^3$/day with a GLR of 3000 led to numerical complications.

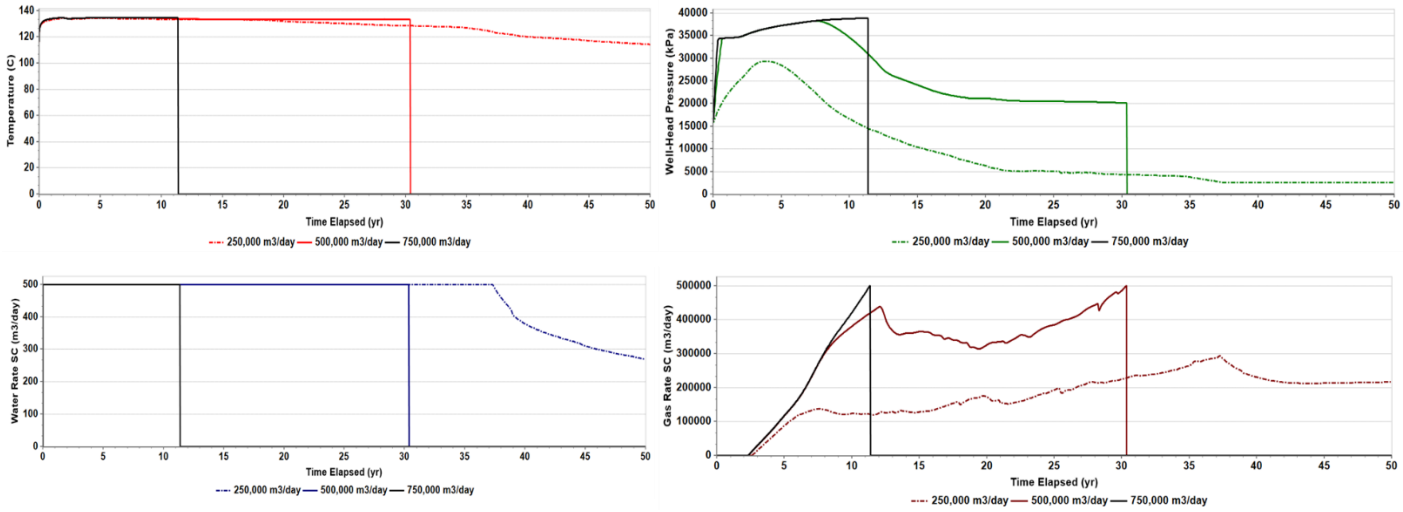


**Figure 41:** Comparison of maximum $CO_2$ injected through Surface Temperature (top left), well-head pressure (top right), water rate (bottom left) and gas rate (bottom right).

## Sensitivity III: Gas-Liquid Ratio

As stated previously, the GLR constraint of 1000 was set in the model, which when reached, the producer would shut-in. The maximum gas liquid ratio reached in our base model was around 800, therefore; lower GLR constraint doesn't have an effect on the production profile, just the time at which the well shuts in. So, the curves at higher GLRs essentially overlap each other as shown in Figure 42.

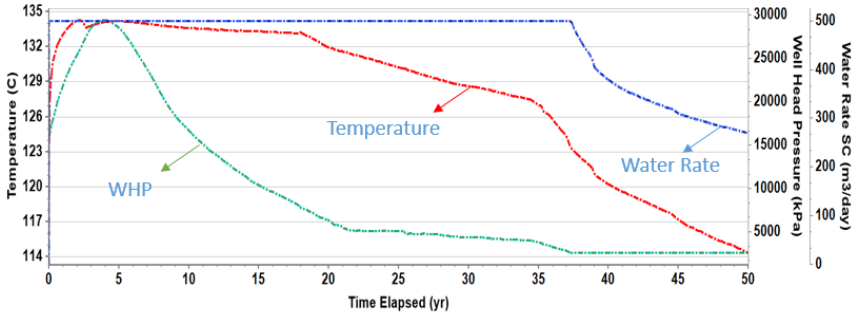


**Gas-liquid ratios of 1000, 2000, 3000 and 5000. The curves overlap.**

**Figure 42:** Impact of increased Gas-Liquid Ratios on the simulation model.

## Conclusions

Geothermal energy, despite being heralded as a viable energy source, has often been overlooked in investment and research initiatives compared to oil and gas. This study has explored geothermal energy as an optimal source of energy extraction from high-temperature aquifers through numerical simulations. Synthetic model simulations were conducted to validate the inputs, and the analysis was extended to a real-field-scale simulation. Additionally, sensitivity analyses were performed to assess the impact of different parameters on the simulation model.

The study showed the feasibility of heat production from deep geopressured geothermal reservoirs (Wilcox) on the Gulf Coast using a conventional injector-producer setup. The results demonstrated the effect of well placement, working fluid type, injection rate, and other factors on heat production over 50 years.

The findings revealed a trade-off between reservoir temperature and produced temperature, highlighting the need for a balance between the production rate and produced temperature. A higher produced temperature leads to a more rapid depletion of reservoir heat. This underscores the importance of simulations in optimizing geothermal extraction strategies. Furthermore, the three most important properties for geothermal efficiency from saline aquifers are: inter-well distance, temperature (geothermal gradient), and injection and production rates.

The use of CO2 as an alternative injection fluid was also explored. While CO2 injection proved to be a less effective fluid, it could present an attractive and profitable opportunity when coupled with the dual objectives of sequestration and geothermal enhancement. This area requires further investigation.

Additionally, a gap was identified in existing studies regarding the impact of wellbore properties—such as heat conductivity and the sizes of tubing, casing, and cement—on geothermal simulations. This lack of research may be attributed to significant convergence issues associated with larger wellbore sizes. Furthermore, the effects of fracturing in saline aquifers could differ significantly from the cases studied, as the reservoir was deliberately not fractured.

## Acknowledgments

The study is funded by Southwest Research Institute Presidential Directions fund. Authors thank the Computer Modeling Group (CMG) for providing the simulation software to the University of Texas at Austin.

## References


Atrens, A. D.; Gurgenci, H; Rudolph, V. $CO_2$ Thermosiphon for Competitive Geothermal Power Generation. Energy & Fuels 2009 23 (1), 553-557 DOI: 10.1021/ef800601z

Batir, J. F. & Richards, M. C. (2020b). Analysis of Geothermal Resources in Three Texas Counties (No. 1291). USDOE Geothermal Data Repository (United States); Southern Methodist University Huffington Department of Earth Sciences.

Batir, J. F. and Richards, M. C. (2020a). Upshur County Geothermal Assessment, Unpublished Report for Clearwater Reserves, LLC by SMU Geothermal Laboratory, Dallas, TX.

Bebout, D. G., Weise, B. R., Gregory, A. R., & Edwards, M. B. (1982). Wilcox sandstone reservoirs in the deep subsurface along the Texas Gulf Coast: their potential for production of geopressured geothermal energy. Report of Investigations No. 117 (No. DOE/ET/28461-T2). Texas Univ., Austin (USA). Bureau of Economic Geology.

Bebout, D.G., B.R. Weise, A.R. Gregory, and M.B. Edwards. "Wilcox Sandstone Reservoirs in the Deep Subsurface along the Texas Gulf Coast - Their Potential for Production of Geopressured Geothermal Energy. Final Report." Office of Scientific and Technical Information (OSTI), October 1, 1979. https://doi.org/10.2172/5357846.

Bhattacharya, S., Bakhshian, S., Hovorka, S., Uroza, C., Hosseini, S., Bump, A., Trevino, R., Olariu, I., and Haagsma, A., 2023, Integrated Petrophysical Studies for Subsurface Carbon Sequestration, Society of Petrophysicists and Well Log Analysts (SPWLA) Annual Logging Symposium, 9 pages, Conroe.

Bhattacharya, Shuvajit, Ken Wisian, Alexandros Savvaidis, and Mike Eros. "Integrated Subsurface Characterization of a Low-Temperature Geothermal Test Site, Gulf Coast, Texas." Second International Meeting for Applied Geoscience & Energy, August 15, 2022, 2007–11. https://doi.org/10.1190/image2022-3745410.1.

Butler, R. (1991) Thermal Recovery of Oil and Bitumen. Prentice-Hall, Englewood Cliffs, 104 p.

Douglas R. Caldwell, Thermal conductivity of sea water,Deep Sea Research and Oceanographic Abstracts,Volume 21, Issue 2,1974,Pages 131-137, ISSN 0011-7471, https://doi.org/10.1016/0011-7471(74)90070-9.

Esposito, A., & Augustine, C. (2012). Recoverable Resource Estimate of Identified Onshore Geopressured Geothermal Energy in Texas and Louisiana:. US Department of Energy, Office of Energy Efficiency and Renewable Energy, National Renewable Energy Laboratory.

Fontanilla, Jerry P., and Khalid Aziz. "Prediction of Bottom-Hole Conditions For Wet Steam Injection Wells." Journal of Canadian Petroleum Technology 21, no. 02 (March 1, 1982). https://doi.org/10.2118/82-02-04.

Ganjdanesh, R., Bryant, S. L., Orbach, R. L., Pope, G. A., & Sepehrnoori, K. (2012). Coupled Carbon Dioxide Sequestration and Energy Production From Geopressured-Geothermal Aquifers. *Carbon Management Technology Conference*. Paper CMTC-151351-MS. https://doi.org/10.7122/151351-MS

Hargis, R. N. (1985). *Geopressured-Geothermal Wilcox Sandstone Reservoirs, Texas Gulf Coast* (DOE/RA/28300-1). U.S. Department of Energy. https://doi.org/10.2172/6486325

Land, L. S., & Fisher, R. S. (1987). Wilcox sandstone diagenesis, Texas Gulf Coast: a regional isotopic comparison with the Frio Formation. Geological Society, London, Special Publications, 36(1), 219-235.

Liu, Yanguang, Zhu, Xi, Yue, Gaofan, Lin, Wenjing, He, Yujiang, & Wang, Guiling. (2015). A review of fluid flow and heat transfer in the $CO_2$-EGS. Journal of Groundwater Science and Engineering, 3(2), 170–175.

Loucks, R. G., and Dutton, S. P., 2019, Insights into deep, onshore Gulf of Mexico Wilcox sandstone pore networks and reservoir quality through the integration of petrographic, porosity and permeability, and mercury injection capillary pressure analyses: AAPG Bulletin, v. 103, no. 3, p. 745–765, http://doi.org/10.1306/09181817366.

Matthews, C.S., and Russell, D.C., 1967, Pressure build up and flow tests in wells: Dallas, Texas, Society of Petroleum Engineers of American Institute of Mining, Metallurgical, and Petroleum Engineers Monograph 1, 158 p.

Poling, B. E., Prausnitz, J. M. and O'Connell, J. P. 2001. Properties of Gases and Liquids, fifth edition. New York, NY, USA: McGraw-Hill Education. https://www.accessengineeringlibrary.com/content/book/9780070116825

Pritchett, J. W. (2009). Enhanced geothermal systems (EGS) with $CO_2$ as heat transmission fluid–A modeling study. Proceedings of the 34th Workshop on Geothermal Reservoir Engineering, Stanford University, Stanford, California, February 9–11, 2009.

Richards, M. C., & Blackwell, D. D. (2012). Developing geothermal energy in Texas: mapping the temperatures and resources. Transactions, Gulf Coast Association of Geological Societies, 62.

Riney, T. D. (1991). Pleasant Bayou Geopressured-Geothermal Reservoir Analysis-January 1991 (No. SSS-TR-91-12162 Draft). DOE EEGTP (USDOE Office of Energy Efficiency and Renewable Energy Geothermal Tech Pgm).

Robinson, B. M., Holditch, S. A., and lee, W. J., 1986, A case study of the Wilcox (lobo) trend in Webb and Zapata Counties, Texas: Journal of Petroleum Technology, v. 38, no. 13,p. 1355-1364

Rowe, A.M.; Chou, J.C.S.: Pressure-volume-temperature-concentration relation of aqueous NaCI solutions. J. Chem. Eng. Data 15, 61–66 (1970). https://doi.org/10.1021/je60044a016

Sharqawy, M.H.; Lienhard, J.H.; Zubair, S.M.: Thermophysical properties of seawater: a review of existing correlations and data. Desalin. Water Treat. 29, 355 (2011)

Somerton, W. H. Thermal properties and temperature-related behavior of rock/fluid systems. Elsevier, 1992.

Spivey, J.; McCain Jr, W.; North, R. Estimating density, formation volume factor, compressibility, methane solubility and viscosity for oilfield brines at temperatures from 0 to 275 C, pressures to 200 MPa and salinities to 5.7 mole/kg. J. Canadian Petroleum Technology, v. 43, n. 7, 2004

Texas Railroad Commission, 2025; https://www.rrc.texas.gov/news/022625-geothermal-press-release

Vinsome, P.K.W., and J. Westerveld. “A Simple Method For Predicting Cap And Base Rock Heat Losses In’ Thermal Reservoir Simulators.” Journal of Canadian Petroleum Technology 19, no. 03 (July 1, 1980). https://doi.org/10.2118/80-03-04.

Wu, Y., & Li, H. (2020). The potential of coupled carbon storage and geothermal extraction in a $CO_2$-enhanced geothermal system: A review. Geothermal Energy, 8(1), 1–20. https://doi.org/10.1186/s40517-020-00173-w